

Neuronal Excitability

# Afterhyperpolarization Promotes the Firing of Mitral Cells through a Voltage-Dependent Modification of Action Potential Threshold

Nicolas Fourcaud-Trocmé,\* Mickaël Zbili,\* Patricia Duchamp-Viret, and  Nicola Kuczewski<https://doi.org/10.1523/ENEURO.0401-21.2021>

Lyon Neuroscience Research Center, CNRS UMR 5292 - INSERM U 1028 - Université Claude Bernard Lyon 1, Centre Hospitalier Le Vinatier - Bâtiment 462 - Neurocampus, 95 Boulevard Pinel, 69675 Bron Cedex, France

## Abstract

In the olfactory bulb, mitral cells (MCs) display a spontaneous firing that is characterized by bursts of action potentials (APs) intermixed with silent periods. Intraburst firing frequency and duration are heterogeneous among MCs and increase with membrane depolarization. By using patch-clamp recording on rat slices, we dissected out the intrinsic properties responsible for this bursting activity. We showed that the threshold of AP generation dynamically changes as a function of the preceding trajectory of the membrane potential. In fact, the AP threshold became more negative when the membrane was hyperpolarized and had a recovery rate inversely proportional to the membrane repolarization rate. Such variations appeared to be produced by changes in the inactivation state of voltage-dependent Na<sup>+</sup> channels. Thus, AP initiation was favored by hyperpolarizing events, such as negative membrane oscillations or inhibitory synaptic input. After the first AP, the following fast afterhyperpolarization (AHP) brought the threshold to more negative values and then promoted the emission of the following AP. This phenomenon was repeated for each AP of the burst making the fast AHP a regenerative mechanism that sustained the firing, AHP with larger amplitudes and faster repolarizations being associated with larger and higher-frequency bursts. Burst termination was found to be because of the development of a slow repolarization component of the AHP (slow AHP). Overall, the AHP characteristics appeared as a major determinant of the bursting properties.

*Key words:* AHP; burst firing; olfactory bulb; patch clamp; rat; sodium channel

## Significance Statement

Mitral cells (MCs) in the olfactory bulb are the main relay of olfactory information toward higher cortical areas, and their firing activity provides a substrate for olfactory information. The MC intrinsic dynamics generate a discharge of action potentials (APs) in burst patterns whose underlying mechanisms are not yet elucidated. Here, we show the importance of the AP afterhyperpolarization (AHP) in this process. The fast AHP component increases the availability of sodium channels, which facilitates the generation of burst discharge. In addition, the late manifestation of the slow AHP component returns the availability of sodium channels to their initial state and leads to the termination of a burst. Overall, we demonstrate that burst properties of MCs are determined by AHP characteristics.

## Introduction

The afterhyperpolarization (AHP) that follows the action potential (AP) is generally seen as an inhibitory mechanism that

limits neuronal activity by promoting firing frequency adaptation and termination of the AP burst (Schwindt et al., 1988; Faber and Sah, 2007; Adelman et al., 2012; Reuveni and

Received September 27, 2021; accepted December 13, 2021; First published March 11, 2022.

The authors declare no competing financial interests.

Author contributions: N.F.-T., M.Z., P.D.-V., and N.K. designed research; N.K. performed research; N.F.-T., M.Z., and N.K. analyzed data; N.F.-T., M.Z., P.D.-V., and N.K. wrote the paper.

Barkai, 2018). The main mechanism underlying AHP is the activation of voltage- and calcium-dependent potassium currents. However, in some neuronal types, such as mitral cells (MCs), the main output neurons of the olfactory bulb, the synaptic transmission also contributes to the AHP shape (Duménieu et al., 2015). Differences in the activation–inactivation kinetics and calcium sensitivity of the different subtypes of potassium channels, underlying AHP, are responsible for a division of its course into three successive components, a fast, a medium, and a slow AHP, that differ in onset times, rise, and decay kinetics (Schwindt et al., 1988; Sah and Faber, 2002; Andrade et al., 2012). The relative contribution of each component evolves during the neuronal discharge, making the AHP shape dependent on the preceding neuronal activity (Duménieu et al., 2015). The inhibitory action of the AHP is generally attributed to the potassium channels that prevent excitatory currents to bring the membrane potential ( $V_m$ ) to the AP threshold (Rubin and Cleland, 2006). This vision may, however, lead to neglecting the possibility that AHP could potentially have a proexcitatory effect through the deinactivation of some voltage-dependent channels, such as calcium T-type and sodium channels (Deister et al., 2009; Cain and Snutch, 2010; Platkiewicz and Brette, 2011; Iyer et al., 2017). Such deinactivation would promote neuronal firing when the  $V_m$  moves back to the resting-state value.

MCs present a spontaneous firing activity that is characterized by AP clusters (i.e., bursts) interspaced by silent periods (Desmaisons et al., 1999). This activity is mainly because of intrinsic membrane properties, since it could be observed in pharmacologically isolated MCs, in olfactory bulb slices (Balu et al., 2004). The cellular mechanisms behind MC bursting activity remain to be elucidated. Balu and Strowbridge (2007) proposed that the burst termination was because of the buildup of the slow AHP during repetitive firing. A computational model refined this idea by proposing that burst termination is not because of the accumulation of classical AHP currents, but rather by the progressive deinactivation of potassium A-type current ( $I_A$ ) along the consecutive AHPs of the burst (Rubin and Cleland, 2006). However, the mechanisms that trigger the burst, maintain the sustained firing, and determine the number of APs or their frequency remain largely unknown.

Here we provide evidence that, through a dynamic change of AP threshold, the modification of  $V_m$  associated with the AHP act both as a burst regeneration process and as a burst termination mechanism. In this way, the AHP characteristics play a pivotal role in determining the firing properties of MCs.

This work was supported by the CNRS, INSERM, and Lyon 1 University.

\*N.F.-T. and Z.M. contributed equally to this work.

Acknowledgements: We thank Marco Canepari for reading the manuscript and giving suggestions.

Correspondence should be addressed to Patricia Duchamp-Viret at [patricia.viret@cnrs.fr](mailto:patricia.viret@cnrs.fr) or Nicola Kuczewski at [nicola.kuczewski@univ-lyon1.fr](mailto:nicola.kuczewski@univ-lyon1.fr).

<https://doi.org/10.1523/ENEURO.0401-21.2021>

Copyright © 2022 Fourcaud-Trocmé et al.

This is an open-access article distributed under the terms of the Creative Commons Attribution 4.0 International license, which permits unrestricted use, distribution and reproduction in any medium provided that the original work is properly attributed.

## Materials and Methods

### Animals

Animal handling was conducted in accordance with the European Community Council Directive 86/609/EEC. Experiments were performed in postnatal day 30 (P30) to P42 male Long Evans rats (Janvier). The animals were maintained on normal light cycle and *ad libitum* access to water and food.

### Slice preparation

Animals were anesthetized with an intraperitoneal injection of ketamine (50 mg/ml) and then decapitated. The head was quickly immersed in ice-cold (2–4°C) carbogenized artificial CSF (ACSF; composition: 125 mM NaCl, 4 mM KCl, 25 mM NaHCO<sub>3</sub>, 0.5 mM CaCl<sub>2</sub>, 1.25 mM NaH<sub>2</sub>PO<sub>4</sub>, 7 mM MgCl<sub>2</sub>, and 5.5 mM glucose, at pH 7.4) oxygenated with 95% O<sub>2</sub> and 5% CO<sub>2</sub>. The osmolarity was adjusted to 320 mOsm with sucrose. The two olfactory bulbs were removed from the cranial cavity and cut into horizontal slices (400 μm thick) using a vibratome (model VT1000s, Leica Biosystems). Slices were then incubated in Gibb's chamber at 30 ± 1°C in modified calcium and magnesium ACSF (2 mM CaCl<sub>2</sub>, 1 mM MgCl<sub>2</sub>).

### Electrophysiological recordings

Slices were transferred into a recording chamber mounted on an upright microscope (Axioskop FS, Zeiss) and perfused with oxygenated ACSF (4 ml/min) at 30 ± 1°C. Neurons were visualized using a 40× objective and an Orca Flash 4.0 camera (Hamamatsu). Measurements were performed with a RK 400 amplifier (BioLogic). Data were acquired with a sampling frequency of 25 kHz on a PC-Pentium D computer using a 12 bit analog/digital to digital/analog converter (Digidata 1440A, Molecular Devices) and PClamp10 software (Molecular Devices). Patch-clamp recordings were achieved with borosilicate pipettes (outer diameter, 1.5 mm; inner diameter, 1.17 mm; Clark Electromedical Instruments), filled with the intracellular solution (131 mM K-gluconate, 10 mM HEPES, 1 mM EGTA, 1 mM MgCl<sub>2</sub>, 2 mM ATP-Na<sub>2</sub>, 0.3 mM GTP-Na<sub>3</sub>, and 10 mM phosphocreatine, at pH 7.3, 290 mOsm). In our experimental conditions, the equilibrium potential of chloride ions (E<sub>Cl</sub>) was –110 mV, and that of potassium ions (E<sub>K</sub>) was –92 mV. The calculated junction potential of 13 mV was corrected offline.

### Data analysis

#### Evoked activity

Experiments were performed in current clamp. A small steady membrane hyperpolarization was ensured by negative current injection to prevent spontaneous firing. For the experiments investigating the relationship between the level of hyperpolarization and the AP threshold, two successive APs were generated by two 3 ms depolarizing current steps applied at 6 s interval; the second step being preceded by membrane hyperpolarization varying in amplitude and duration. Some data were excluded from the analysis when the average resting potential, in the 500 ms preceding the depolarizing step, differed by >2 mV between the two evoked APs. In experiments investigating the relationship between the speed of

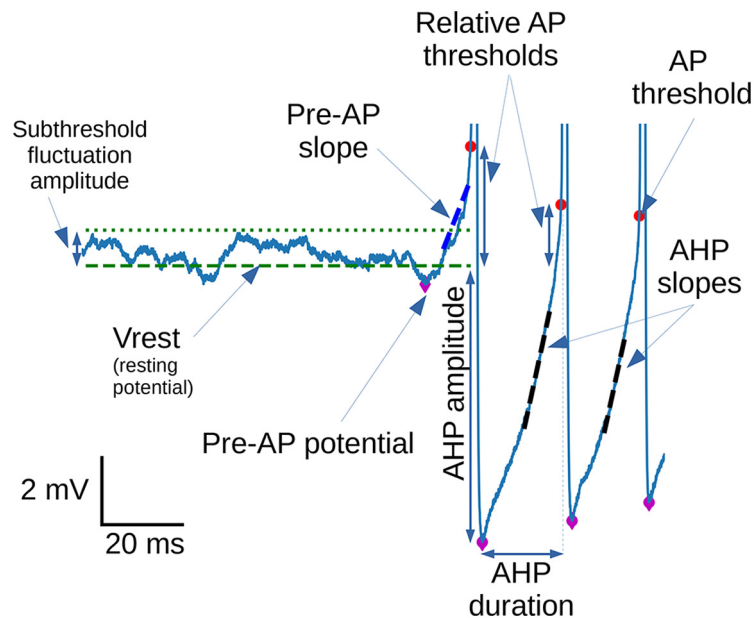


**Figure 1.** Schematic description of the main measurements performed on spontaneous bursts during the study. Red dots represent the thresholds of APs. Purple diamonds represent the most hyperpolarized value of  $V_m$  before one given spike (namely, “pre-AP potential” before the first AP and “AHP peak” before the other APs).

repolarization–hyperpolarization and AP threshold, current ramps of variable slopes were applied. The AP threshold was calculated from the first AP generated during the ramp: it was defined as being the first point with a strict positive acceleration (second derivative of its  $V_m$ ) during the AP rising phase, before it reaches its maximum depolarizing rate.

#### Sodium current measurements

Experiments were performed in voltage clamp in the presence of 0.3 mM cadmium, 4 mM nickel, 10 mM tetraethylammonium, 10 mM 4-aminopyridine (4AP), 10 mM 2,3-dihydroxy-6-nitro-7-sulfonyl-benzo[*f*]quinoxaline, 5 mM 2-aminophosphonovalerate (APV), and 5 mM bicuculline.

#### Spontaneous activity

Spontaneous activity was recorded from cells at their resting membrane potential (17 cells with a resting potential at approximately  $-60$  mV, and 15 cells at approximately  $-55$  mV; see Figs. 2, 3, 6–8). In some cells, we needed to inject a small steady depolarizing current to bring the MP from approximately  $-60$  to approximately  $-55$  mV to generate spontaneous-like activity (15 cells), while in two cells we needed to inject a small hyperpolarizing current to transform tonic firing to burst firing. We did not observe any qualitative differences among all groups of cells in our analyses; they are thus pooled in the description of results.

APs were detected each time the membrane potential crossed  $-23$  mV (detection potential) from below, and the minimum interspike interval (ISI) was set at 1 ms. In one cell, the detection potential was set at  $-43$  mV because of the low amplitude of the first AP in bursts.

Bursts were detected based on a time-interval threshold for the ISIs (tISIs), below which two occurring APs

were assigned to the same burst. To achieve this, the tISI was first set at 90 ms for all analyzed MCs, and then adapted cell by cell in a recursive manner through the following procedure: we computed a new tISI as the median ISI of all detected bursts in a cell, plus four times their median absolute deviation (except for one cell: only 0.8 times its median absolute deviation; cell label 8 in the figures). If the new tISI was lower than the previous one, we used it again to detect bursts of the cell and restart over a new tISI computation and so on, until the new tISI was larger than the last one (final burst ISI thresholds: mean, 47 ms; SD, 19 ms; range, 13–90 ms). The reliability of the burst detection method was assessed by visual inspection of traces. In our analyses, we will always refer to the burst size as the number of APs within each burst.

In the following, we describe how AP parameters or burst parameters used in this study were measured. An example of  $V_m$  trace with a schematic of most of the measures of interest is shown in Figure 1.

Because some recorded MCs showed slow fluctuations of subthreshold  $V_m$ , the latter was computed before each burst. If the interval without an AP preceding a burst (interburst interval) lasted at least 200 ms, we defined the burst resting potential ( $V_{rest}$ ) as the median  $V_m$  during the interburst interval (excluding half of the tISI at the beginning and 5 ms at the end). We also defined subthreshold fluctuation amplitude as the maximum  $V_m$  on the same interval. If the interburst interval lasted  $<200$  ms,  $V_{rest}$  and subthreshold fluctuation amplitudes were defined as the same as for the preceding burst. In some figures (see legends), traces are aligned on  $V_{rest}$ , which was then set at 0 mV.

For each detected AP, we computed its voltage threshold (AP threshold) as the first point with a strictly positive acceleration (second derivative of  $V_m$ ) during the AP rising phase before  $V_m$  reaches its maximum positive acceleration rate.

In this study, we often used the relative AP threshold defined as the difference between AP threshold and  $V_{rest}$ .

The pre-AP potential was the first negative  $V_m$  peak that preceded the AP threshold. It was detected by stepping backward in time starting from the AP threshold by 1 ms steps and by stopping as soon as a  $V_m$  rebound of at least 0.4 mV (relative to the lowest  $V_m$  in the interval from current time step up to AP threshold time) was found. The pre-AP potential was defined as the lowest  $V_m$  between the rebound time and the AP threshold time.

The pre-AP slope was the slope of the  $V_m$  course preceding the first AP of the burst. When pre-AP potential occurred  $>5$  ms before the AP threshold time, the pre-AP slope was obtained by a linear regression of the  $V_m$  course during the 5 ms before the AP threshold. When the pre-AP potential occurred  $<5$  ms before AP threshold, the pre-AP slope was obtained by a linear regression of  $V_m$  course in a range of 20–80% from the pre-AP potential (0%) to the AP threshold (100%).

AHP amplitude was calculated by making the difference between the lowest  $V_m$  between two consecutive APs (or in the 300 ms following the AP, if the ISI was too long) and  $V_{rest}$ . Note that, according to our convention, the AHP amplitudes are negative numbers.

The AHP slope was defined as the slope of a linear regression of  $V_m$  between the AHP peak and the next AP threshold, but restricted to a 20–60%  $V_m$  range starting from the AHP peak (0%) up to the previous AP threshold potential (100%). The  $V_m$  range for linear regression was indeed based on the preceding AP, to allow computation of the AHP slope following the last AP of a burst in the same way as the AHP slopes within the burst.

The AHP duration was defined as the period from the AHP peak to the next AP threshold time. The intraburst frequency was defined as the average of the inverse ISIs within the burst.

We noticed that, following a burst, a slow AHP component induced a slow repolarization of the  $V_m$  toward  $V_{rest}$ . To quantitatively characterize this component for each MC, we selected all bursts with a following interburst interval of at least 500 ms. Electrophysiological traces were aligned on the AHP peak following the last AP, and a median trace was calculated. We then fitted this median trace from 50 to 500 ms after the AHP peak with a single exponential that gave the slow AHP time constant. Because of our choice of a minimum interval of 500 ms, some cells had no burst selected for median computation, the fit was thus possible in only 42 of the 49 cells used in this study.

#### *Synaptically evoked activity*

Experiments were performed in current clamp at MC resting membrane potential. Synaptic activity was produced by 0.1 ms electrical stimulation (8–10 mA) of the olfactory nerve layer that was produced by a bipolar electrode. Firing analysis was performed as for spontaneous activity.

#### **Threshold linear model**

To predict the expected AP threshold following the last burst AP, for each cell, we fitted a model of intraburst AP

threshold as a linear combination of AHP amplitude, AHP slope, AHP duration, and  $V_{rest}$  using an ordinary least squares regression method. Note that we also tested models taking into account interactions between these parameters, but the increase in fit reliability (based on the Bayesian information criterion) was negligible and did not justify taking these interactions into account.

Once a model was fitted for a given cell, we could predict the expected AP threshold following the last AP of each burst as a function of time elapsed after the last AHP maximum time (which gave the AHP duration parameter, with other model parameters being constant).

#### **Burst size and burst frequency linear models**

To quantify the dependence of burst size and burst frequency on fast and slow AHP parameters, we pooled data from all cells and fitted models of burst size and burst frequency as a linear combination of  $V_{rest}$ , AHP amplitude, and AHP slope (both measured during the first AHP within the burst) and their interactions. Linear models were fitted using an ordinary least squares regression method. Two additional models, including the slow AHP time constant (measured once for each cell as stated above), were fitted and statistically compared with the previous models with type I ANOVAs. Only bursts of more than three APs were included in this analysis. Normality and heteroscedasticity of residuals were checked visually and were required to transform the endogenous variables before model fitting as follows:  $\log(\log(\text{burst size}))$  and  $\log(\text{burst frequency})$ .

#### **Neuron computational model**

A single compartment model was simulated with NEURON 7.8. All simulations were run with 100- $\mu$ s time steps. The nominal temperature was 30°C. The voltage dependence of activation and inactivation of Hodgkin–Huxley-based conductance models were taken from the study by Hu et al. (2009) for  $\text{Na}_v$  and delayed rectifier potassium channels (KDR), and from the study by Rubin and Cleland (2006) for  $I_A$ . The equilibrium potentials for  $\text{Na}^+$ ,  $\text{K}^+$ , and passive channels were set to +90, –91, and –28.878 mV, respectively. We began by constructing a model with the following conductance densities: 0.02, 0.0002, 0.003, and  $3.33 \times 10^{-5}$  S/cm<sup>2</sup> for  $\text{Na}_v$ , KDR,  $I_A$ , and passive channels, respectively. This model presented a resting membrane potential of –60 mV without holding current injection. In all the other model configurations, we injected a holding current during the simulation to maintain the resting membrane potential at –60 mV.

No  $I_A$  conductance was implemented in the model (see Fig. 5). The conductance density of  $\text{Na}_v$  was set to 0.02, 0.005, or 0.0025 S/cm<sup>2</sup>. The holding current was set to –0.826, –29.49, and –29.26 pA, respectively. Spikes were induced by 3 ms positive current steps of 400 pA. Hyperpolarizations before APs were induced by 50 ms negative current steps whose amplitudes were set to obtain a pre-AP membrane potential from –60 to –70 mV. AP threshold was defined by the voltage point at which the first-time derivative ( $dV/dt$ ) went  $>40$  mV/ms. The curve of



AP threshold versus pre-AP activatable  $\text{Na}_v$  conductance was constructed by varying  $\text{Na}_v$  conductance density from 0.04 to 0.0025 S/cm<sup>2</sup>, inducing one spike from resting membrane potential and measuring AP threshold. The values of pre-AP activatable  $\text{Na}_v$  conductance were obtained by multiplying the percentage of noninactivated  $\text{Na}_v$  conductance—just before the positive current step—by the total  $\text{Na}_v$  conductance density.

For the figure 9 simulations, the  $\text{Na}_v$  conductance density was set to 0.02 S/cm<sup>2</sup>. The  $I_A$  conductance was either directly taken from the study by Rubin and Cleland (2006) or modified to get the biophysics values closer to previously published  $I_A$  biophysics values (Amendola et al., 2012). The modifications were done on the inactivation of  $I_A$  conductance: modified  $I_A$  displayed a more depolarized half-inactivation (−90 mV instead of −110 mV), a larger slope of inactivation curve (0.1 mV<sup>−1</sup> instead of 0.056 mV<sup>−1</sup>), and a shorter inactivation time constant (50 ms instead of 150 ms). The holding current to keep the resting membrane potential at −60 mV was −30.826 pA for no  $I_A$  condition, 0 pA for  $I_A$  condition, and −5.85 pA for  $I_A$  modified condition. Spikes were induced by 3 ms positive current steps of 1 nA. Trains of spikes were induced by trains of these current steps, at 40 Hz.

### Statistical analysis

In many cases, we computed correlations between the different parameters characterizing the burst dynamics. We generally computed and plotted the within-cell correlations. Summary plots (mainly presented as extended data) show, for each cell, the slope of the correlation (left part of the figure), the strength of the correlation ( $R$  of the linear regression; right part of the figure). Single-cell statistically significant correlations ( $p < 0.05$ , corrected for multiple comparisons with the Bonferroni–Holm methods) are shown in dark blue (for both the slope and strength of the correlation). Global population statistical analysis was performed on the slopes and correlation coefficients of individual cells using standard  $t$  tests, assessing that the population averages were different from 0. Whisker plots give minimum and maximal values (whiskers), second and third quartile (box), and outliers calculated as deviations  $>1.5 \times \text{IQR}$  (interquartile range) from the first and third quartiles (diamonds). If not stated differently in results, the text gives the mean  $\pm$  95% confidence interval (CI; defined as  $1.96 \times \text{SEM}$ ). Boxes show the mean and 95% confidence interval of the mean. Other quantities of interest are effect sizes (ESs), correlation coefficients ( $R$ ),  $t$  values and  $p$ -values from  $t$  tests on  $R$  values, and the number of cells used in the analyses ( $N$ ). Note that  $p$ -values from  $t$  tests performed on slopes are only given in figures. Bayesian analysis was performed with JASP Team (2020) by using the default effect size prior (Cauchy scale = 0.707).

### Exclusion criteria

Twenty-three spontaneously active MCs were excluded from the analysis based on the following reasons: 5

showed poor recording, 3 showed only continuous tonic activity, 11 showed too few bursts ( $<4$  bursts), 2 had too high membrane resistance to be identified as MCs ( $>500 \text{ M}\Omega$ ), and 2 presented burst intervals too short to compute resting potential ( $< 200 \text{ ms}$ ).

### Software

All analyses were performed with custom Python 2.7 scripts, using the statistical or curve-fitting functions from Scipy 1.2.2, and the multiple comparison functions or multiple regression functions from StatsModels 0.9.0.

### Code accessibility

Computational neuron model has been run with the software NEURON on a Linux personal computer. The corresponding code is freely available at the following address: <https://osf.io/9bgxp/>.

### Data availability

All raw electrophysiological traces, scripts for trace analyses, data analyses, and models scripts are available at Open Science Framework (<https://osf.io/s2dbw/>).

## Results

### Heterogeneity of spontaneous firing activity between different MCs

Whole-cell recordings were performed on 72 spontaneously active MCs in olfactory bulb slices obtained from 21 rats between the ages of 30 and 42 d. Among recorded cells, 23 were excluded from the analysis based on criteria detailed in Materials and Methods. As previously shown (Chen and Shepherd, 1997; Desmaisons et al., 1999; Balu et al., 2004), firing activity was characterized by clusters of APs, henceforth denominated bursts, separated by silent periods presenting subthreshold membrane oscillations (Fig. 2A). A total of 1532 bursts (with at least 2 APs) and 386 isolated APs were analyzed. Burst properties such as the number of APs, the membrane potential at which bursts occurred, interburst frequency, and intraburst frequency were heterogeneous (Fig. 2B–E, left). Such heterogeneity could be partly because of specific differences among the recorded MCs (Fig. 2B–E, right), in which population intrinsic biophysical diversity is shown (Padmanabhan and Urban, 2010), but also because of the difference in the average holding potential (i.e.,  $V_{\text{rest}}$ ) between the different MCs. In fact, more depolarized MCs presented higher intraburst frequency ( $R = 0.58$ , Wald test;  $p < 0.001$ ;  $N = 49$ ; data not shown) and larger burst size (i.e., larger number of APs in burst;  $R = 0.38$ , Wald test;  $p = 0.007$ ;  $N = 49$ , data not shown). Burst size and intraburst frequency ( $R = 0.56$ , Wald test;  $p < 0.001$ ;  $N = 49$ , data not shown) were also positively correlated. It should be noted that the  $V_{\text{rest}}$  distribution is bimodal (see Materials and Methods), but because such a bimodality was not expressed in other burst parameters, all cells were pooled in subsequent analyses.

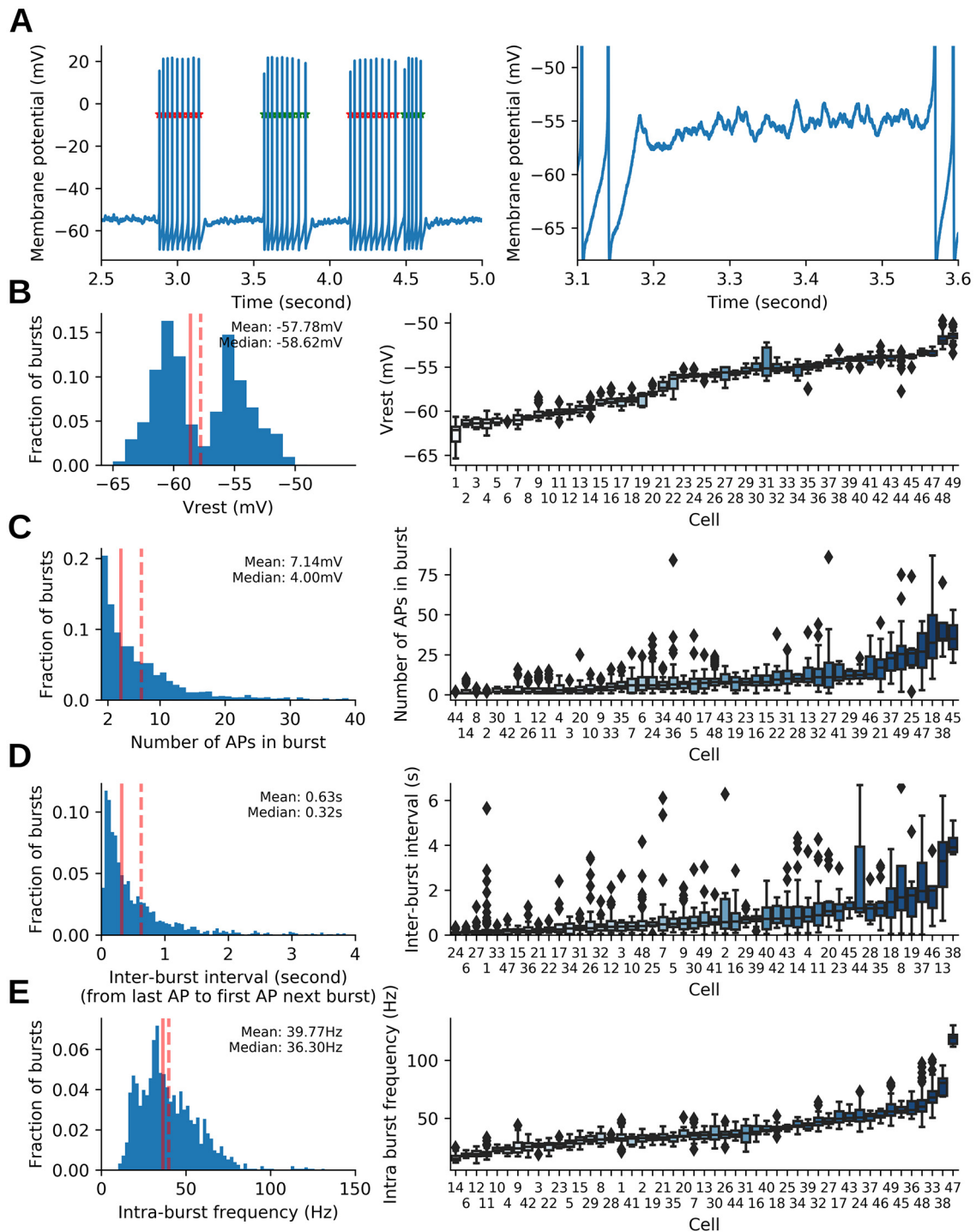


**Figure 2.** Burst properties of MCs. **A**, Left, Example of spontaneous recording in MCs showing typical bursts of APs. APs belonging to the same burst are alternatively identified by red and green stars. Right, Enlargement of the trace in **A**, left, showing  $V_m$  dynamics with fast oscillations, which were typical during interburst periods. **B**, Distribution of  $V_m$  values preceding bursts ( $V_{rest}$ ). Left, Distribution for all detected bursts. Right, Whisker plot per cell showing intercell variability. **C**, Distribution of burst sizes (number of APs in bursts, left and right: same representation as in **B**). **D**, Distribution of interburst intervals (same representation as in **B**). **E**, Distribution of intraburst frequencies (left and right: same representation as in **B**). **B-E**, Left panels, Continuous and dashed vertical lines materialize the median and mean values, respectively. **B-E**, Right panels, diamonds correspond to outliers, calculated as deviations  $>1.5 \times IQR$  from the first and third quartiles.

## Dynamic modulation of AP threshold at resting potential

In cortical neurons, the AP threshold is affected by the trajectory of  $V_m$  that precedes the AP. In particular, when the  $V_m$  is hyperpolarized or the rate of membrane depolarization ( $dV_m/dt$ ) preceding the AP is faster, a more negative AP threshold is observed (Henze and Buzsáki, 2001; Azouz and Gray, 2003; Li et al., 2014). Similarly, in MCs, the AP threshold is more negative when firing is preceded by  $V_m$  hyperpolarization induced by negative current injection (Balu et al., 2004). Interestingly, during spontaneous firing the initiation of a burst was always preceded by hyperpolarization of the  $V_m$  (Fig. 3A,B, example), which is in agreement with a previous report (Desmaisons et al., 1999). We therefore investigated whether the oscillatory activity, potentially associated with the spontaneous inhibitory transmission, was capable of producing a dynamic modification of AP threshold contributing to the firing initiation. In MCs, the threshold of the first AP of a burst was driven toward more negative values by a stronger hyperpolarization of  $V_m$  preceding the burst, which is hereafter called pre-AP potential (for its calculation, see Materials and Methods and Fig. 1). The average modification of AP threshold was  $-0.37 \pm 0.94$  mV for 1 mV pre-AP potential hyperpolarization (ES = 1.13,  $R = 0.48 \pm 0.08$ ,  $t = 11.6$ ,  $p < 0.001$ ,  $N = 49$ ; Fig. 3C). We then analyzed the depolarization rate of  $V_m$  preceding the first AP, called here the pre-AP slope (Fig. 3B, examples; for its calculation, see Materials and Methods and Fig. 1). By contrast to what was reported for cortical neurons and predicted by theoretical models (Platkiewicz and Brette, 2011), in MCs, a larger pre-AP slope preceding the burst was associated with a more depolarized AP threshold (0.85  $\pm$  0.71 mV, an increase in AP threshold per 1 mV/ms increase in pre-AP slope; ES = 0.34,  $R = 0.18 \pm 0.07$ ,  $t = 4.96$ ,  $p < 0.0001$ ,  $N = 49$ ; Fig. 3D). This unexpected effect may be a consequence of the small positive covariation we measured between the pre-AP potential and the pre-AP slope [lower pre-AP slope for more hyperpolarized pre-AP potential; average slope,  $0.04 \pm 0.02$  (mV/ms)/mV; ES = 0.52;  $R = 0.13 \pm 0.07$ ;  $t = 3.41$ ;  $p = 0.0013$ ;  $N = 49$ ; data not shown]. According to the literature, this covariation should induce opposite effects on the threshold potential. Therefore, the pre-AP potential effect appeared to prevail over the pre-AP slope effect.

Since the AP threshold of MCs can dynamically shift depending on the recent history of  $V_m$ , it is conceivable that the firing could be induced by hyperpolarizing events bringing the AP threshold below the median  $V_{rest}$  (for its calculation, see Materials and Methods and Fig. 1) or within the range of sub-threshold  $V_m$  oscillations. This was indeed the case for 27% of recorded bursts (representing 92% of recorded MCs). Unsurprisingly, the level of hyperpolarization (pre-AP potential  $-V_{rest}$ ) preceding the burst was larger in these cases (Fig. 3E, left, example) than in bursts where the threshold of the first AP remained above the  $V_{rest}$  (Fig. 3E, right, example; hyperpolarization,  $-1.30 \pm 0.17$  vs  $-0.56 \pm 0.07$  mV;  $t = -9.48$ ;  $p < 0.001$ ; ES = 0.44;  $N = 513$  and 1405; data not shown). Altogether, these data suggest that spontaneous firing in MCs could be triggered according to the following two

modalities: (1) a membrane hyperpolarization produced by the oscillatory and/or inhibitory synaptic activity that brings the AP threshold below  $V_{rest}$  or within  $V_{rest}$  variability (Fig. 3E, left); and (2) a classical membrane depolarization above the  $V_{rest}$ , eventually produced by the excitatory synaptic activity (Fig. 3E, right).

## Cellular mechanisms of AP threshold modification

The relationship between  $V_m$  and AP threshold was further investigated in the experiment depicted in Figure 4. Here MCs were slightly hyperpolarized with a steady current injection to prevent spontaneous firing, and two successive APs were evoked at 6 s intervals by short (3 ms) depolarizing current steps, with the second AP being preceded by a 50 ms hyperpolarizing current step (Fig. 4A, left). The comparison of AP thresholds between the two evoked APs showed that pre-AP membrane hyperpolarization produced a linear shift of AP threshold toward more hyperpolarized values ( $-0.32 \pm 0.05$  mV threshold shift per each millivolt of membrane hyperpolarization; Fig. 4A, right;  $N = 75$ ). The same effect was obtained with pre-AP hyperpolarization duration varying over a range from 10 to 90 ms (Fig. 4B;  $N = 16$ ). The contribution of the membrane depolarization rate to AP threshold was evaluated by comparing the effect of depolarizing ramps at different speeds (Fig. 4C, left). For the recorded MCs ( $N = 11$ ), a faster depolarization rate leads to more negative AP thresholds (Fig. 4C, right). The slope of the linear regression obtained from AP threshold/depolarizing speed analysis showed a shift of AP threshold of  $-7 \pm 3$   $\mu$ V for each millivolt per millisecond in membrane-depolarizing speed (Fig. 4C; right; ES =  $-1.2$ ,  $p = 0.003$ ). Therefore, similar to what was observed in cortical neurons (Henze and Buzsáki, 2001; Azouz and Gray, 2003; Li et al., 2014), AP threshold in MCs became more negative when  $V_m$  was depolarized with a fast depolarization rate. This result supports the interpretation that the opposite correlation between AP threshold and pre-AP slope during spontaneous firing (Fig. 3D) would be a consequence of a more hyperpolarized pre-AP potential when the pre-AP slope is lower.

The most likely mechanism responsible for the modification of the threshold produced by membrane hyperpolarization is the recovery from inactivation of voltage-dependent channels implicated in AP generation; namely, the  $\text{Na}^+$  and T-type  $\text{Ca}^{2+}$  channels. To test this assumption, we used the same experimental procedure as described in Figure 4A, combined with a pharmacological approach as well as a computational neuron model. Since the pharmacological compounds were applied at different time periods, we first assessed that the effect of membrane hyperpolarization on AP threshold effect was stable over time by testing it 5 and 10 min after the beginning of the recording (Extended Data Fig. 5-1C,D). To investigate the effect of the recovery from inactivation of  $\text{Na}_v$  channels on AP threshold decrease, we first used a simple computational neuron model containing only one  $\text{Na}_v$  channel type and one  $\text{K}_v$  delayed-rectifier channel type (see Materials and Methods for details). This model closely mimicked the shift of AP threshold produced by



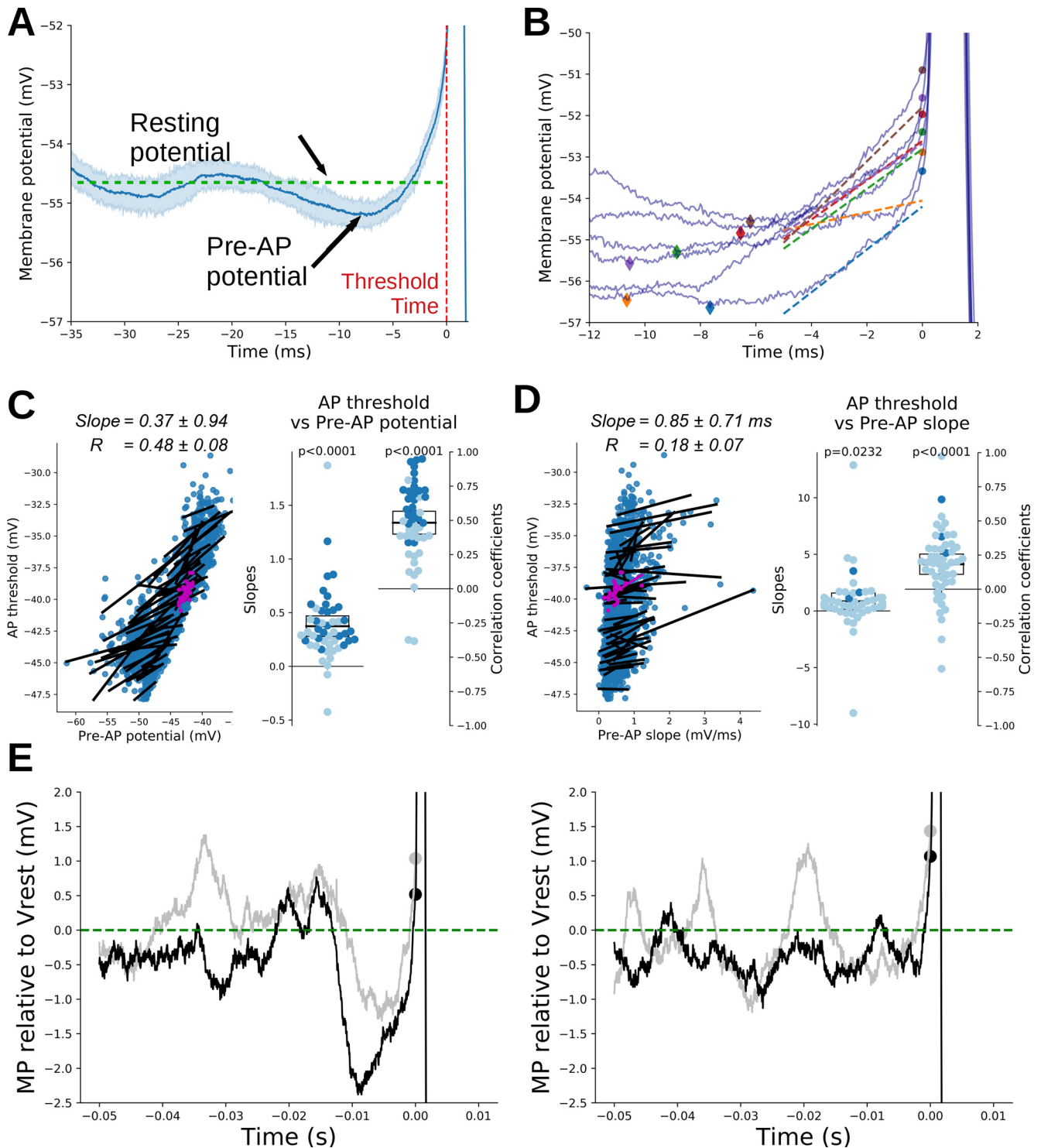


**Figure 3.** The threshold of the first AP of the burst is affected by the  $V_m$  trajectory before threshold. **A**, Bursts were often initiated after a hyperpolarization phase of the  $V_m$  (pre-AP potential). Here,  $V_m$  traces preceding each burst of a single neuron (neuron #32) were averaged (blue line) along with their SD (shaded area). **B**, Example of the variability of pre-AP slope and first AP threshold in the same cell (neuron #32). For each trace, a diamond marks the pre-AP potential, a round dot marks the first AP threshold, and a dashed line marks the pre-AP slope (lines are displayed in the time interval where  $V_m$  was fitted). Each color corresponds to one given trace. Note that a more negative threshold value corresponds to a more hyperpolarized pre-AP potential. See Materials and Methods and Figure 1 for the details of each measure. **C**, AP threshold positively correlated with pre-AP potential. Left panels, Correlations between the pre-AP potential and first AP threshold. A linear fit was performed for each neuron (one dot per burst, the fit is shown as a black line). In purple are the measurements and fit of the neuron exemplified in **A** and **B**. Average slope and average correlation across neurons are displayed above (mean  $\pm$  SEM,  $N=49$  MCs). Right panels, Scatter plots of the slopes (left) and



continued

correlation coefficients (right) obtained from the linear fit done for each neuron in the left panel. Darker dots correspond to individual fits with  $p < 0.05$  (Pearson correlation, corrected for multiple comparisons). Black boxes show the mean and its 95% confidence interval for each distribution. The significance of deviation from 0 of each distribution was further tested with a one-sample  $t$  test ( $p$ -values are displayed above each scatter plot; see main text and Materials and Methods for additional details). **D**, Small positive correlation between the  $V_m$  slope preceding the first burst AP (pre-AP slope) and the first AP threshold. Data are presented as in **C**. **E**, Left, Examples (black and gray lines) of strong membrane hyperpolarization bringing the AP threshold (large dots) within the range of membrane fluctuations. Right, Examples of AP threshold that remained above membrane fluctuations. For comparison, traces were aligned on  $V_{rest}$  (set at 0 for the figure). All four examples come from the same recording (neuron #24).

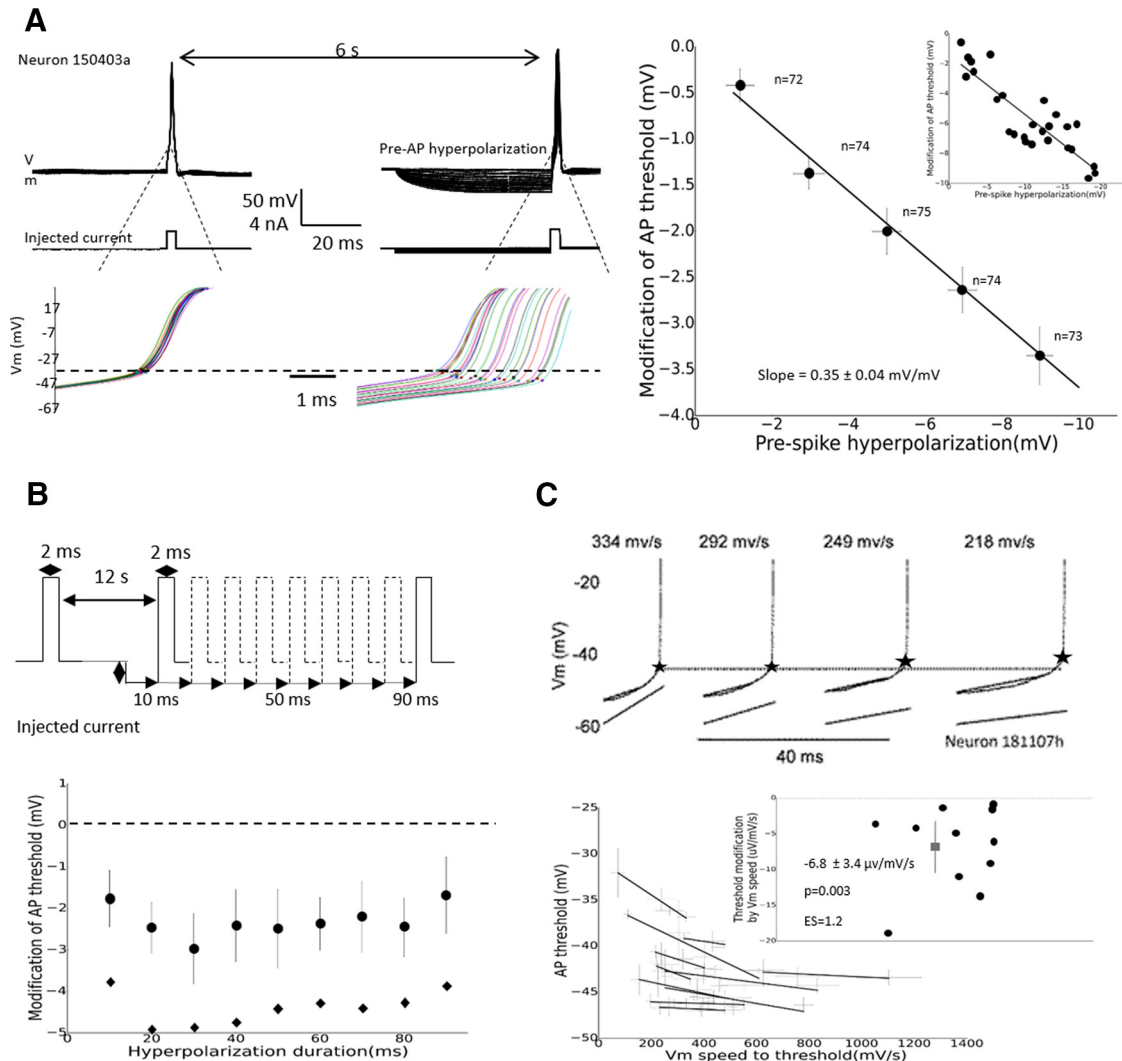


**Figure 4.** AP threshold of MCs decreased with membrane hyperpolarization and high depolarization speed. **A**, AP threshold decreased proportionally with membrane hyperpolarization. Left, Experimental protocol and representative example of threshold modification by membrane hyperpolarization. Dots show AP thresholds, dashed line shows the threshold position in the absence of hyperpolarization. Right, Quantification of spike threshold modifications produced by membrane hyperpolarization. Inset, Analysis performed on neuron 150403a is depicted on the left. The number of cells is given above each point. **B**, Spike threshold modification was not affected by the duration of membrane hyperpolarization. Top, Schematic representation of the experimental protocol. Bottom, Quantification of the effect ( $N = 16$  MCs). Black circles, Average AP threshold modification; gray diamonds, average membrane hyperpolarization (same scale as threshold modification). **C**, AP threshold decreased with the membrane depolarization rate. Top, Experimental protocol and representative examples of AP thresholds for different depolarization rates. Stars show the threshold position; lower lines materialize depolarization current ramps (only the last 10 ms preceding the threshold is shown). Bottom, Quantification of AP threshold as a function of membrane depolarization rate for 11 MCs. Inset, Quantification of AP threshold modification as a function of membrane depolarization rate for the 11 MCs. Horizontal and vertical bars represent 95% confidence interval.

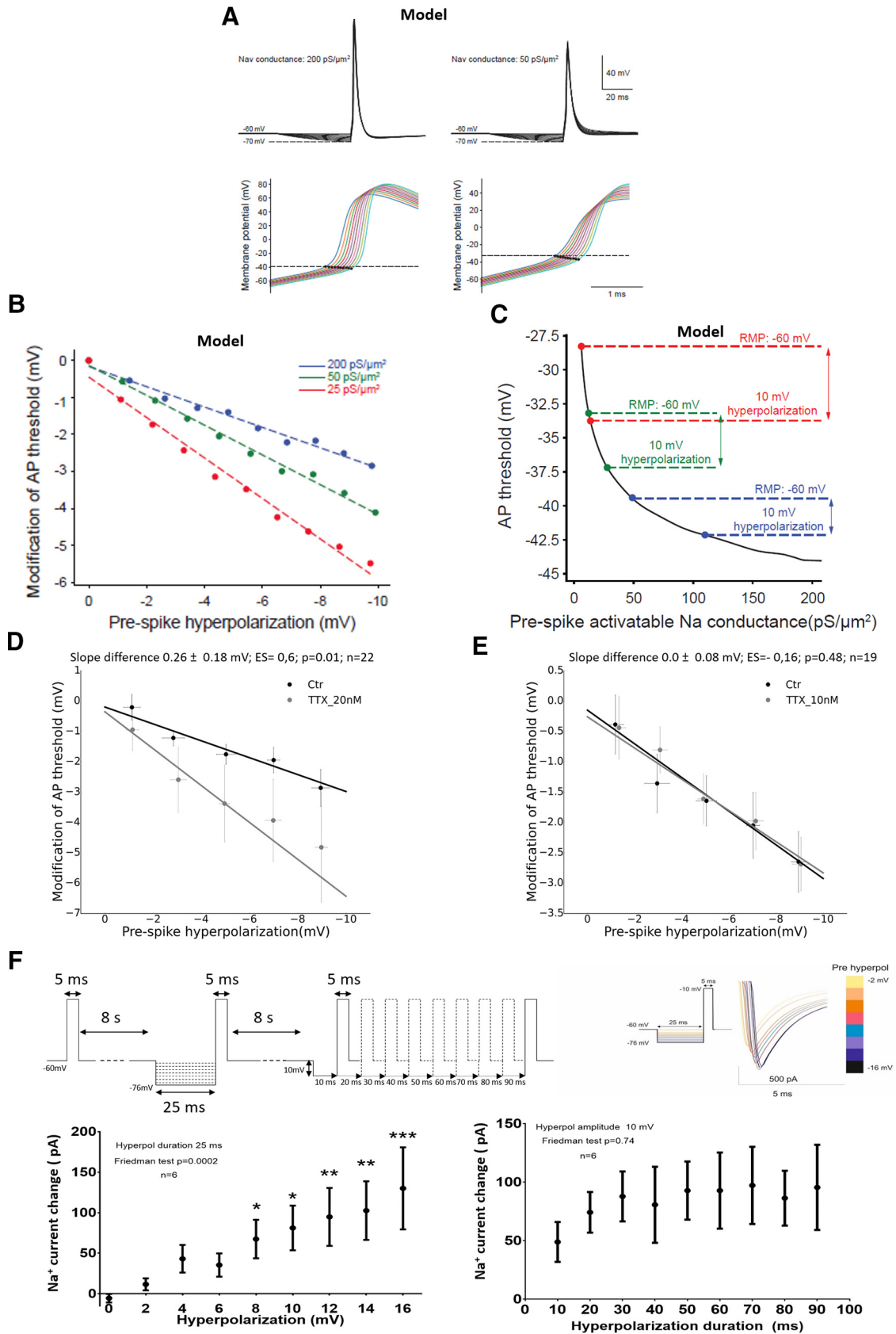


**Figure 5.** Sodium but not calcium channels participate in the modification of the AP threshold induced by membrane hyperpolarization. **A**, Neuron model simulation showing the modification of AP threshold with membrane hyperpolarization for high  $\text{Na}_v$  density

continued

(200 pS/ $\mu\text{m}^2$ ) and low  $\text{Na}_v$  density (50 pS/ $\mu\text{m}^2$ ). Bottom panels are enlargements of top panels. AP thresholds are marked by black dots. **B**, Quantification in the neuron model of the effect of membrane hyperpolarization on AP threshold for different  $\text{Na}_v$  channels densities. Note an amplification of the AP threshold shift induced by membrane hyperpolarization when the density of  $\text{Na}_v$  channels was reduced. **C**, Curve depicting the modification of AP threshold in the neuron model as a function of the quantity of  $\text{Na}_v$  conductance activatable before the AP. Note that the same 10 mV membrane hyperpolarization produced a stronger modification of AP threshold when the density of  $\text{Na}_v$  channels was reduced (compare the following three conditions: 200, 50, and 25 pS/ $\mu\text{m}^2$ ). **D**, TTX at 20 nM amplified the AP threshold shift induced by membrane hyperpolarization. **E**, TTX at 10 nM failed to amplify the AP threshold shift produced by membrane hyperpolarization. **F**, Membrane hyperpolarization resulted in an amplification of  $\text{Na}^+$  current in MCs. Top left, Experimental protocol depicting the imposed modifications of membrane voltage. Top right, Representative of  $\text{Na}^+$  current following membrane hyperpolarization. Bottom left, Quantification of the modification induced by different levels of membrane hyperpolarization on  $\text{Na}^+$  current amplitude. Bottom right, Quantification of the modification produced, by different duration of membrane hyperpolarization, on  $\text{Na}^+$  current amplitude. \* $p < 0.02$ ; \*\* $p < 0.01$ ; \*\*\* $p < 0.001$ , *post hoc* comparisons with the condition without hyperpolarization, Dunn's test. Bars represent the 95% CI in **A**, **E**, and **F**, and the SEM in **G**. More details on pharmacological protocol, time stability of AP threshold, and effect of the voltage-dependent  $\text{Ca}^{2+}$  channel antagonist can be found in Extended Data Figure 5-1.

the membrane potential hyperpolarization (Fig. 5A, left and 5B, blue). Thus, the shift could be attributable to the recovery from inactivation of  $\text{Na}_v$  channels produced by the  $V_m$  hyperpolarization, leading to a hyperpolarization of AP threshold. To observe the effect of the partial blockade of  $\text{Na}_v$  channels, we decreased the density of  $\text{Na}_v$  channels to 50 and 25 pS/ $\mu\text{m}^2$ . As expected, decreasing the density of  $\text{Na}_v$  channels in the model, led to a shift of AP threshold toward more positive values (Fig. 5A, right). More interestingly, under reduced  $\text{Na}_v$  condition (50 and 25 pS/ $\mu\text{m}^2$ ), the hyperpolarization of membrane potential resulted in a larger decrease of AP threshold than in the control condition (Fig. 5B; note that the slope of the curve hyperpolarization/threshold shift became larger when the  $\text{Na}_v$  channels density is decreased). This can be explained by taking into account that the AP threshold is not linearly correlated with the quantity of activatable  $\text{Na}_v$  channels. Figure 5C shows the curve of the AP threshold versus the quantity of activatable  $\text{Na}_v$  conductance, just before the AP occurrence. On this curve, we plotted the following: the quantity of  $\text{Na}_v$  conductance activatable at  $V_{\text{rest}}$  (−60 mV) or after 10 mV hyperpolarization (−70 mV) for the three conditions of  $\text{Na}_v$  channels density (200 pS/ $\mu\text{m}^2$  in red, 50 pS/ $\mu\text{m}^2$  in green, or 25 pS/ $\mu\text{m}^2$  in blue). We can see that the increase in the availability of  $\text{Na}_v$  channels, produced by  $V_m$  hyperpolarization, is associated with a greater decrease of AP threshold in reduced  $\text{Na}_v$  condition (50 or 25 pS/ $\mu\text{m}^2$ ) than in the control condition (200 pS/ $\mu\text{m}^2$ ). The prediction of the model was checked by applying low doses of the Na channel blocker TTX (10 or 20 nM). The availability of  $\text{Na}_v$  channel was reduced by TTX at these doses, as assessed by the positive shift of AP threshold (Extended Data Fig. 5-1B). In agreement with the model prediction, the effect of membrane hyperpolarization on AP threshold was amplified by TTX at 20 nM (Fig. 5D; difference between threshold/hyperpolarization slopes in control and TTX 20 nM:  $0.26 \pm 0.18$  mV/mV; ES = 0.6;  $p = 0.01$ ;  $N = 22$ ). Interestingly, this effect was not observed with TTX at 10 nM (Fig. 5E; difference between threshold/hyperpolarization slopes in control and TTX 10 nM:  $-0.03 \pm 0.18$  mV/mV; ES =  $-0.16$ ;  $p = 0.48$ ;  $\text{BF}_{10} = 0.3$ ; evidence of absence,  $N = 19$ ). This result suggests that, at approximately −60 mV, the recovery from inactivation produced by the hyperpolarization would

mainly involve the  $\text{Na}_v$  channel subtypes blocked by [TTX] > 10 nM (see Discussion). The participation of T-type  $\text{Ca}^{2+}$  channels was also investigated by using the selective antagonist ML218 (5–10  $\mu\text{M}$ ). As shown in Extended Data Figure 5-1E, ML218 did not modify the shift of AP threshold induced by membrane hyperpolarization (difference between threshold/hyperpolarization slopes in control and ML218:  $-0.0 \pm 0.1$  mV/mV; ES = 0.1;  $p = 0.66$ ;  $N = 21$ ), indicating that this effect was not based on recovery from the inactivation of T-type  $\text{Ca}^{2+}$  channels. We finally determined whether, in MCs recorded close to  $V_{\text{rest}}$  (−60 mV), short hyperpolarization of  $V_m$  could produce a recovery from the inactivation of  $\text{Na}^+$  channels. To this end, we performed the experiment depicted in Figure 5F. Here,  $\text{Na}^+$  current was pharmacologically isolated (see Materials and Methods) and MCs were recorded in voltage-clamp configuration. Following the short membrane prehyperpolarization (25 ms), the amplitude of  $\text{Na}^+$  current generated by a 5 ms depolarization step to −10 mV, increased proportionally to the hyperpolarization level ( $p = 0.0002$ ,  $N = 6$ , Friedman test). Moreover, the recovery from the inactivation of  $\text{Na}^+$  channels was independent of the duration of the hyperpolarization, in the 10–90 ms range ( $p = 0.74$ ,  $N = 6$ , Friedman test). These results echoed the effects produced by membrane hyperpolarization on AP threshold that were depicted in Figure 4, A and B, further supporting the hypothesis that the threshold shift was based on the recovery from inactivation of  $\text{Na}^+$  channels.

### Spontaneous bursting activity was promoted by dynamic modification of AP threshold induced by AHP

We next investigated the impact of dynamic modifications of AP threshold on MC firing during the burst. As shown in Figure 6A, the AP thresholds within the bursts were naturally shifted to more negative potentials than those of the first AP (delta difference in threshold between the first and second AP in the burst =  $-2.28 \pm 0.09$  mV;  $N = 1532$  bursts; ES =  $-1.28$ ;  $t = -50.0$ ;  $p < 0.001$ ; Fig. 6B). The most likely explanation of the threshold shift within the burst is the membrane hyperpolarization induced by the preceding AHP. Indeed, the modification of AP threshold shift, calculated between the first and the second AP of the bursts, positively correlated with the

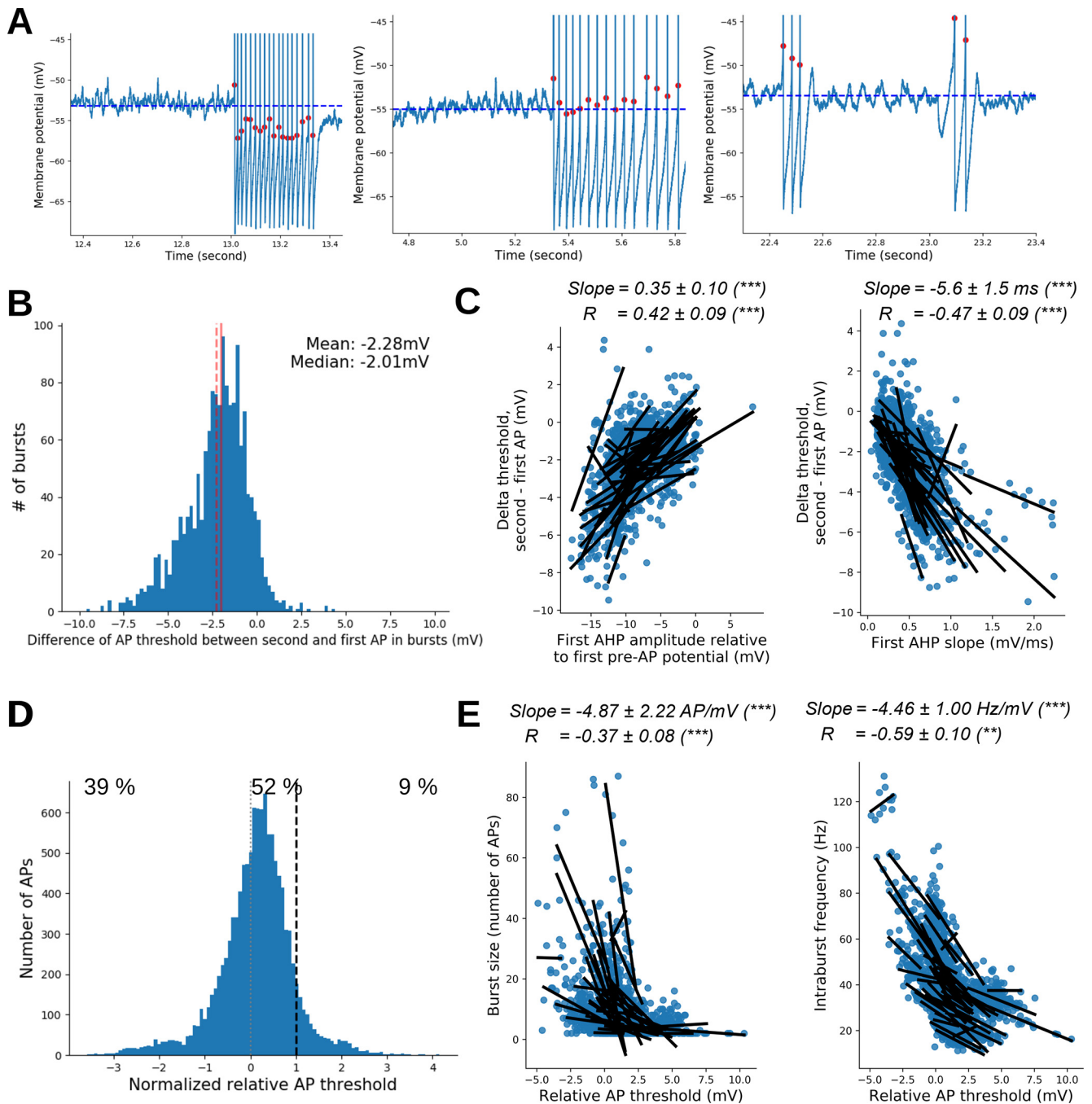


**Figure 6.** The AHP-induced hyperpolarization lowered the AP threshold within the bursts and determined the firing properties. **A**, Examples illustrating the lowering of threshold for APs within the burst. The dashed line is  $V_{\text{rest}}$ . Note that in the left and middle panels AP threshold is shifted below  $V_{\text{rest}}$  or inside  $V_m$  fluctuations, respectively. In right panel, the rebound of  $V_m$  observed after the AHP could potentially allow the burst generation despite the high AP threshold relative to  $V_{\text{rest}}$ . **B**, Histogram of differences in AP threshold between the second and the first AP of the bursts. Continuous and dashed vertical lines materialize the mean and median values, respectively. **C**, AHP properties determine the negative shift of AP threshold. Left, Larger AHP produced a larger negative shift of AP threshold. Positive correlation between the difference of the second and first AP threshold and the first AHP amplitude (computed here relative to the first pre-AP potential). Right, Faster AHP repolarization produced larger hyperpolarization of AP threshold. Negative correlation between the difference of the second and first AP threshold and the first AHP slope. **D**, Distribution of the AP threshold relative to  $V_{\text{rest}}$  (first AP of each burst is excluded), normalized so that 1 (dashed line) corresponds to the maximum  $V_m$  reached during rest. **E**, More negative values of relative AP thresholds were associated with bursts having a higher number of APs (left) and higher intraburst frequencies (right). Results in **C** and **E** are presented as in Figure 3C. See Extended Data Figures 6-1 and 6-2 for statistical details and individual-cell fit results. The relationship between AHP characteristics and firing properties can be found in Extended Data Figure 6-3. Examples of the characteristics of evoked firing can be found in Extended Data Figure 6-4.



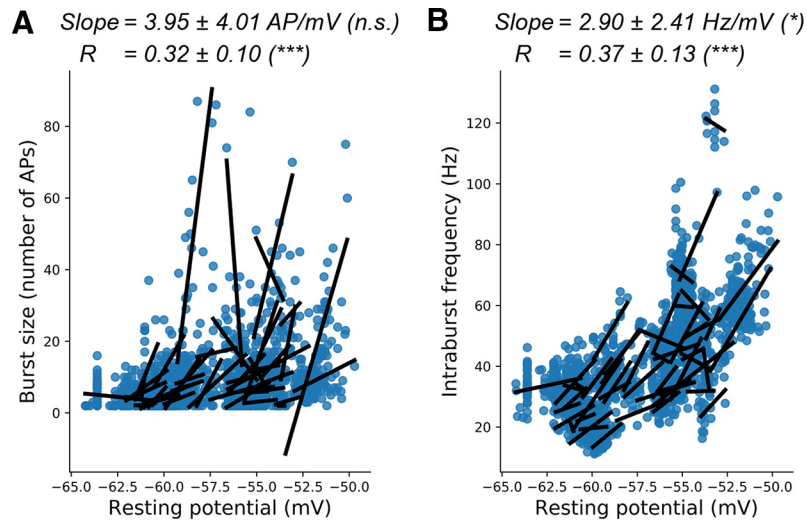


**Figure 7.** Influence of resting potential on burst size and frequency. **A, B**, Linear fits between burst firing properties and resting potential preceding the burst ( $V_{rest}$ ); results are presented as in Figure 3C. **A**, Burst size (number of APs) increased with  $V_m$  depolarization. **B**, Intraburst frequency increased with  $V_m$  depolarization. Statistical details and single-cell fit results are shown in Extended Data Figure 7-1, A and B.

AHP amplitude, measured here relative to the first pre-AP potential ( $-0.35 \pm 0.10$  mV of AP threshold shift for each millivolt of membrane hyperpolarization; Fig. 6C, left), as well as with the repolarization rate of the AHP ( $-5.6 \pm 1.5$   $\mu$ V of AP threshold shift for each millivolt per second of modification of membrane depolarizing speed; Fig. 6C, right). These results suggested that both the AHP amplitude and repolarization rate accounted for the negative AP threshold shift within the burst. Interestingly, this effect, observed at the single-cell level, was also seen at the population level, by looking at average values per cell (Extended Data Fig. 6-1C,D). Once the first AP fired from resting potential, the AP threshold shift, induced by AHP, could act as a regenerative mechanism of firing, especially when it drove the threshold below the  $V_{rest}$  (Fig. 6A, left) or within the range of spontaneous membrane oscillations (Fig. 6A, middle). To precisely assess the position of AP thresholds relatively to subthreshold fluctuations, we normalized the thresholds of intraburst APs (i.e., all the APs except the first one) using a linear interpolation. We set  $V_{rest}$  at 0 and the maximum amplitude of the subthreshold fluctuations at 1. We called this measure the “normalized relative AP threshold.” In such conditions, a negative value for the normalized AP threshold meant that it was more hyperpolarized than  $V_{rest}$ , a value between 0 and 1, which meant that it was within the range of  $V_m$  intrinsic subthreshold fluctuations and a value  $>1$  meant that it was more depolarized than subthreshold fluctuations. As shown in Figure 6D, AP threshold was more negative than  $V_{rest}$  for 39% of intraburst APs: it remained within the range of subthreshold membrane oscillations for 52% and, above membrane oscillatory activity, for the remaining 9%. A clear heterogeneity of the normalized relative AP threshold was observed between MCs (Extended Data Fig. 6-2A). Interestingly the AP threshold shift relative to the  $V_{rest}$  (relative AP threshold), appeared to affect bursts properties. Stronger negative

shifts were associated with burst having higher numbers of APs (Fig. 6E, left) and higher intraburst firing frequency (Fig. 6E, right). A similar correlation was observed between the average intraburst AP relative threshold in different MCs and their average burst sizes and intraburst frequency (Extended Data Fig. 6-2C).

As expected from the relationship between the AHP and AP threshold shift, the intraburst firing properties correlated with AHP properties. Larger AHP amplitudes were associated with longer bursts and higher firing frequencies (Extended Data Fig. 6-3A1,B1). In addition, faster AHP repolarizations were associated with longer bursts and higher firing frequencies (Extended Data Fig. 6-3C1,D1). We also observed that the speed of repolarization of AHP more strongly impacted MC firing properties than AHP amplitude. A similar contribution of AHP to MC firing properties was observed when performing between-cell analyses (Extended Data Fig. 6-3A2, B2,C2,D2), suggesting that firing heterogeneity among the different MCs reported in Figure 1 are, at least partly, based on the heterogeneity of their AHP characteristics with a predominant role of the AHP slope.

By using electrical stimulation of the olfactory nerve, synaptically evoked firing was induced in two MCs. As shown in Extended Data Figure 6-4, the evoked firing-induced bursts in these cells had similar properties to spontaneous ones, except that subthreshold EPSP lasted longer than the AP duration. These preliminary results suggest that, once APs are generated, the bursting characteristics of MCs are determined by their intrinsic biophysical properties (i.e., the AHP), regardless of the modality of AP induction.

So far, we provided evidence that the frequency and spike number of MC bursts were affected by the negative shift of AP threshold produced by the AHP, through the recovery from inactivation of  $\text{Na}^+$  channels. However, the burst properties depend also on the  $V_{rest}$ . In fact, the frequency and spike number of MC bursts were increased

when  $V_{rest}$  was depolarized (Fig. 7). This effect was likely because of the stronger negative shift of AP threshold within the burst when the  $V_m$  was depolarized (Extended Data Fig. 7-1C). The following three factors could support the latter effect: (1) an increase in AHP amplitude with  $V_m$  depolarization (Extended Data Fig. 7-1D), possibly because of the increase in  $K^+$  driving force with the membrane depolarization; (2) an increase in AHP repolarization speed of the AHP with  $V_m$  depolarization (Extended Data Fig. 7-1E); and (3) a stronger effect of  $Na_v$  channel recovery from inactivation, because of increased steady-state inactivation when the  $V_m$  was depolarized. Indeed, in the simple neuron computational model, a depolarization of the  $V_m$  led to a partial inactivation of  $Na_v$  channels, a reduction of the quantity of prespike activatable  $Na_v$  channels, and therefore a greater effect of  $V_m$  hyperpolarization on AP threshold shift (Extended Data Fig. 7-1G,H). The third factor is experimentally supported by the observation that the slope of the correlation between relative AP threshold and AHP amplitude was larger for depolarized MCs (i.e., for the same AHP amplitude, the AP threshold negative shift is larger for depolarized  $V_m$ ; Extended Data Fig. 7-1F). Overall, the three factors could cooperate to make the relative AP threshold more negative, thus making the bursts longer and faster for the more depolarized  $V_m$ . All these effects, shown here at the cellular level, were also observed at the population level (cell-to-cell analysis; data not shown).

### The evolution of the late slow component of the AHP contributed to the burst termination

A plausible mechanism that could account for the burst termination is the evolution of the AP threshold along the burst bringing this parameter above the  $V_{rest}$ . However, although a small positive shift of the AP threshold was observed along the bursts (Fig. 8A, left; increase of normalized threshold: mean,  $0.053 \pm 0.027$  mV; paired  $t$  test,  $t = 3.83$ ;  $p < 0.001$ ;  $N = 1276$ ; ES = 0.11), the AP threshold remained largely below, or within, the range of  $V_m$  subthreshold oscillation (Fig. 8A, right). The small evolution of AP threshold probably reflected the small decrease of absolute AHP amplitude and the small slowing down of the AHP repolarization rate along the bursts (Extended Data Fig. 8-1). To further clarify the mechanisms of burst termination, we used a linear model (using  $V_{rest}$ , AHP amplitude, AHP slope, and AHP duration as parameters; see Materials and Methods for details) that predicts the dynamics of the putative AP threshold after the last AP of the burst (Fig. 8B, red dashed lines, examples). This analysis showed that, for 89% of the bursts, the  $V_m$  that followed the last AP did not overcome the putative threshold (Fig. 8C, left). Such an effect cannot be explained by an overestimation of the threshold by the model since, at a time interval equal to the last interspike interval, the predicted threshold was similar to the threshold of the last AP of the burst (Fig. 8C, right; difference of potential between last AP threshold and predicted threshold, 0.09 mV; SD, 0.68 mV;  $N = 1532$  bursts). Indeed, the failure of  $V_m$  to overcome the AP threshold appears to be because of the modification of the AHP, in which a late, slow

repolarizing component develops following the early fast repolarizing component characterizing the intraburst AHP. This new AHP component could be fitted with a slow exponential (time constant: mean, 171.66 ms; SD, 88.76 ms;  $N = 42$  MCs; Fig. 8D,E; Balu and Strowbridge, 2007, their Fig. 2C). This component kept the  $V_m$  more hyperpolarized than during the intraburst AHPs, preventing the  $V_m$  to reach the AP threshold. This result suggests a scenario where the AP threshold can only be reached during the early fast component of the AHP repolarization phase, with the onset of the late slow AHP repolarization preventing the  $V_m$  from reaching a threshold moving rapidly to preburst values.

Thus, the termination of burst discharge seems to be attributable to the onset of a slow component during the repolarizing phase of the AHP. To investigate how this slow component develops along the burst, we performed the experiment depicted in Figure 9. Here MCs were slightly hyperpolarized with a steady current injection, preventing spontaneous firing, while trains of APs were evoked by short (3 ms) depolarizing-current steps at 40 Hz. Five trains of 1, 2, 4, 8, and 16 APs, respectively, were generated, and the parameters of the last AHP were compared (Fig. 9A). As shown in Figure 9, C and D, the AHP amplitude and area increased with the number of APs (repeated-measures ANOVA,  $p < 0.001$ ;  $N = 11$ ). Interestingly, the slow AHP component appeared at more and more hyperpolarized  $V_m$  as the number of APs increased (repeated-measures ANOVA,  $p < 0.001$ ;  $N = 11$ ; Fig. 9E). This result suggests that, in spontaneous bursts, the probability that the fast AHP repolarizing component can overcome the AP threshold decreases along the AP sequence until it is no longer able to produce further APs. The slow late AHP component is reminiscent of the slow inactivating  $K^+$  current that was previously observed in MCs following membrane hyperpolarization and that was suggested to be produced by the recovery from inactivation of the  $I_A$  current (Balu and Strowbridge, 2007, their Fig. 5). The hypothesis that the slow AHP component is because of the deinactivation of the  $I_A$  current during fast AHP is further supported by a computational model of MCs showing that this current increases during the AP burst (Rubin and Cleland, 2006). Indeed, the application of 4AP (3 mM; Fig. 9B) prevented the evolution of AHP during the evoked AP trains (AHP area: 4AP effect,  $p = 0.005$ ; interaction,  $p < 0.001$ ; AHP amplitude: 4AP effect,  $p = 0.002$ ; interaction,  $p < 0.001$ ; Fig. 9C,D) as well as the negative shift of  $V_m$  at which the slow AHP component appears (4AP effect,  $p = 0.004$ ; interaction,  $p < 0.001$ ; Fig. 9E). Note that 4AP reduced both the early-fast and late-slow AHP. The hypothesis that the slow component involves the activation of  $I_A$  current is further supported by our neuron model (Fig. 9F). In fact, in the simple model involving only  $Na_v$  and KDR channels, there was no development of a slow AHP component when the number of APs increased (Fig. 9F, left, no  $I_A$ ). However, the implementation of  $I_A$  current to the model reproduced the development of a slow AHP with the number of APs, as observed in our recordings (Fig. 9F,  $I_A$  and  $I_A$  modified). The conductance of  $I_A$  was either directly taken from (Rubin and Cleland, 2006) or was modified, to get the biophysics

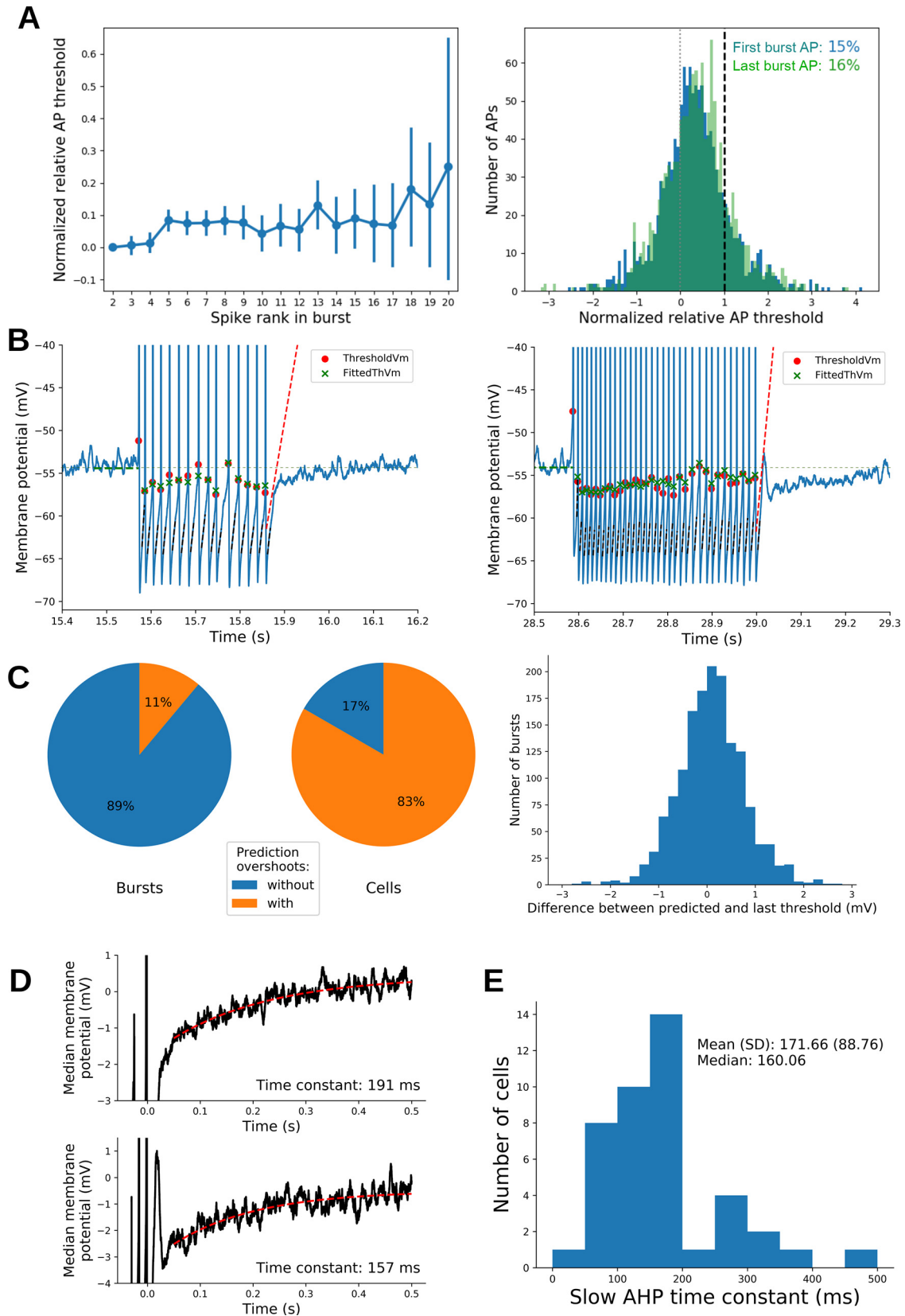


**Figure 8.** Bursts are terminated by the onset of a slow AHP component. **A**, Left, Evolution along the burst of the normalized AP threshold (linear interpolation between 0 and 1, which were the resting potential and the maximum amplitude of subthreshold fluctuations, respectively). To compare between bursts, data were shifted and aligned at 0 for the second AP threshold. We observed a clear but small increase of normalized AP threshold during a burst. Right, Histograms of normalized AP thresholds for the second

*continued*

AP (blue) and last AP (green) in bursts (left panel). Percentiles give the proportion of data  $>1$ . **B**, Examples of bursts with a detected AP threshold (red dots) and their model fits (green cross). Dashed red lines set the predicted threshold as a function of time elapsed after the beginning of the last AHP. We noted that bursts could be either followed by postburst rebound (right) or not (left). In both cases, the  $V_m$  stayed below the predicted AP threshold, accounting for the end of the burst, and a sudden decay of  $V_m$  repolarization rate was observed. See text and Materials and Methods for the model details. **C**, As shown in **B**, we could detect when the  $V_m$  goes above the predicted threshold (overshoot) without producing a further AP. Left, Pie chart shows the proportion of bursts with a predicted overshoot (pooled across cells). Middle, Pie chart shows the proportion of cells with at least one predicted overshoot among their bursts. Right, Distribution of the differences between predicted AP threshold (at the same ISI as the last burst ISI) and the threshold of the last AP in the burst. **D**, Median traces of the 500 ms following the last AHP peak with exponential fits of the slow AHP component (computed from 50 to 500 ms following AHP peak). Top and bottom correspond to cells shown in **B**, left and right, respectively. **E**, Distribution of the time constant of the exponential fits shown in **D** for all 42 cells (see Materials and Methods for details). The evolution of the AHP characteristics along the burst can be found in Extended Data Figure 8-1.

closer to previously published  $I_A$  biophysics (Amendola et al., 2012; see Materials and Methods). Noteworthy is that the  $I_A$  current is minimal at the AHP peak and then increases again during the repolarization phase of the fast AHP, leading to the development of the slow AHP component (Fig. 9F, bottom panels). Altogether, these data suggest that, in MCs, the burst is stopped by the buildup of the 4AP-dependent,  $I_A$ -like current that, by slowing down the AHP, brings the AP threshold to values that cannot be reached during  $V_m$  repolarization.

### The fast AHP features from the first spike of the burst and slow AHP dynamics are informative about intraburst frequency and burst size

Altogether, our experiments suggested that, in MCs, the burst frequency is determined by the fast AHP component while the burst termination (and thus the burst size) is determined by the development of the slow AHP during the burst. Therefore, we decided to observe whether the features of the fast and slow AHP, measured respectively after the first and the last AP of the burst, are good predictors of burst dynamics.

First, we only considered  $V_{rest}$  and fast AHP features. Pooling data from all cells (but only from bursts with at least three APs), we used linear models to predict burst size (number of APs) and within-burst frequency based on the following:  $V_{rest}$ , fast AHP amplitude, and fast AHP depolarization rate measured after the first AP of each burst (see Materials and Methods for model details). The models showed that burst frequency clearly depends on all parameters and their interactions ( $R^2 = 0.69$ ;  $F_{(10,1081)} = 410.9$ ;  $p < 0.0001$ ;  $N = 1092$  bursts). A similar but smaller effect was observed for burst size ( $R^2 = 0.27$ ;  $F_{(10,1081)} = 66.3$ ;  $p < 0.0001$ ;  $N = 1092$  bursts). Thus, fast AHP dynamics following first AP is more informative of burst frequency than burst size.

Then, we also considered slow AHP features by introducing, in the linear models, the average time constant of the slow AHP (measured once in each cell; Fig. 8E). It should be noted that what we expected to be important in controlling the burst termination was the development of the slow AHP during the successive APs of the burst, but this could not be measured from the traces of spontaneous bursting activity. We therefore assumed that the development of the slow AHP correlated with its average time constant, which we could measure at the

end of the burst. The addition of the mean time constant of the slow AHP to the linear model independent variables significantly improved their fitting performance, in particular in burst length (ANOVA comparisons of models with and without the time constant of the slow AHP as parameter: frequency:  $F_{(4,1081)} = 28.6$ ,  $p < 0.0001$ ; burst size:  $F_{(4,1081)} = 25.5$ ,  $p < 0.0001$ ;  $R^2$  of the new linear models and effect size ( $f^2$ ) between models: frequency:  $R^2 = 0.72$ ,  $f^2 = 0.03$ ; burst size:  $R^2 = 0.33$ ,  $f^2 = 0.06$ ).

Overall, the linear model analysis confirmed that the burst properties largely depend on the characteristics of the initial fast AHP and  $V_{rest}$ , the slow AHP impacting the termination of the burst, and, thus, the burst size.

## Discussion

Our study provides new insights into the understanding of the intrinsic cellular mechanisms responsible for the genesis of firing activity in MCs. More precisely, we have shown that AHP plays a key role in this genesis since changes in its characteristics (duration, amplitude, kinetics) can both trigger and stop the burst generation while also determining the bursting properties. The experimental results presented in this report have been synthesized to build the toy model described in Figure 10. The firing of MC is triggered by a modification of the AP threshold that dynamically changes as a function of the  $V_m$  trajectory (Fig. 10A). Because of the relatively depolarized  $V_{rest}$  of MCs, a part of the voltage-dependent  $Na^+$  channels is inactivated. Hyperpolarization of  $V_m$  because of intrinsic oscillatory activity and/or synaptic inputs leads to  $Na_v$  channel deinactivation, bringing the AP threshold within  $V_m$  subthreshold fluctuations, thus facilitating the firing. Once the first AP is generated, the following fast AHP brings the threshold below the  $V_{rest}$ , or within the  $V_{rest}$  noise, acting in this way as a regenerative mechanism that will produce the burst (Fig. 10B). The burst termination is ensured by a slow, 4AP-dependent AHP component that progressively develops along the consecutive APs and is hypothesized to involve the  $I_A$  current. This component slows down the AHP repolarization phase, and thus increases the inactivation of  $Na_v^+$  channels and moves back the AP threshold to values that cannot be overcome by  $V_m$  repolarization. The intraburst properties (frequency, length) are determined by the magnitude of the modification of the AP threshold relative to



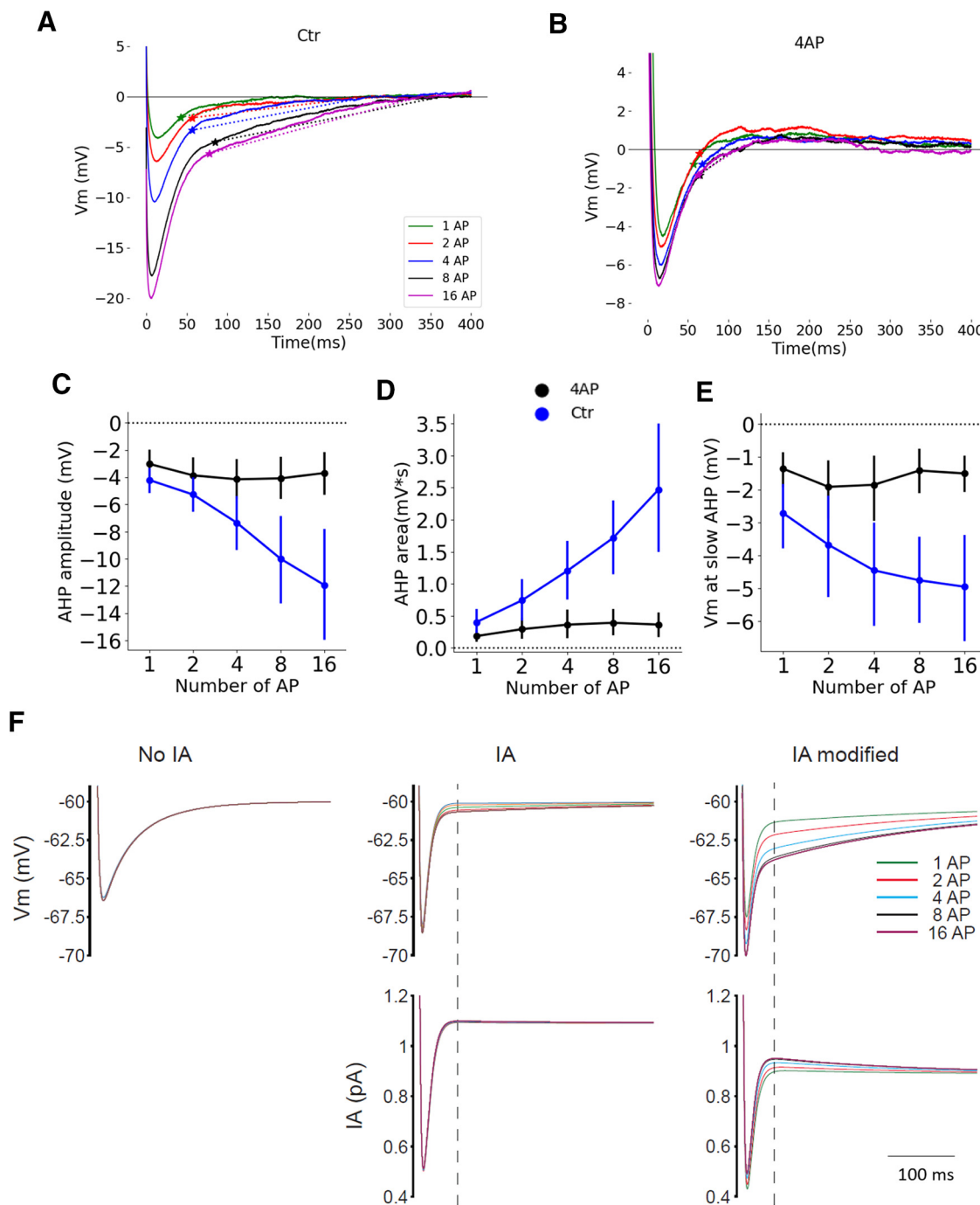


**Figure 9.** The AHP evolution with the number of APs was mainly because of 4AP-sensitive component. **A**, Superposition of the last AHP of evoked trains comprising a different number of APs. Stars indicate the onset of the slow AHP component (i.e., at which the “ $V_m$  at slow AHP” was measured). **B**, Same neuron as **A** but in the presence of 4AP (3 mM). **C**, Modification of AHP, as a function of the number of APs in the trains, in the control condition and in the presence of 4AP. **D**, Modification of the AHP area, as a function of the number of APs in the trains, in the control condition and in the presence of 4AP. **E**, Modification of the  $V_m$  at which the slow component appeared, as a function of the number of APs in the bursts, in the control condition and in the presence of 4AP. **F**, Neuron model showing the superposition of the last AHP at the end of evoked trains comprising different numbers of APs. Top Left, with only  $Na_v$  and KDR channels in the model, there was no evolution of the AHP with the number of APs. Top middle and right, Adding  $I_A$  current in the model reproduced the evolution of the slow AHP observed in experimental data. Bottom, Evolution of  $I_A$  current during the AHP.  $I_A$  channels biophysics from the study by Rubin and Cleland (2006);  $I_A$  modified, channels biophysics closer to those in the study by Amendola et al. (2012). Error bars represent 95% confidence intervals.  $N = 11$  MCs.

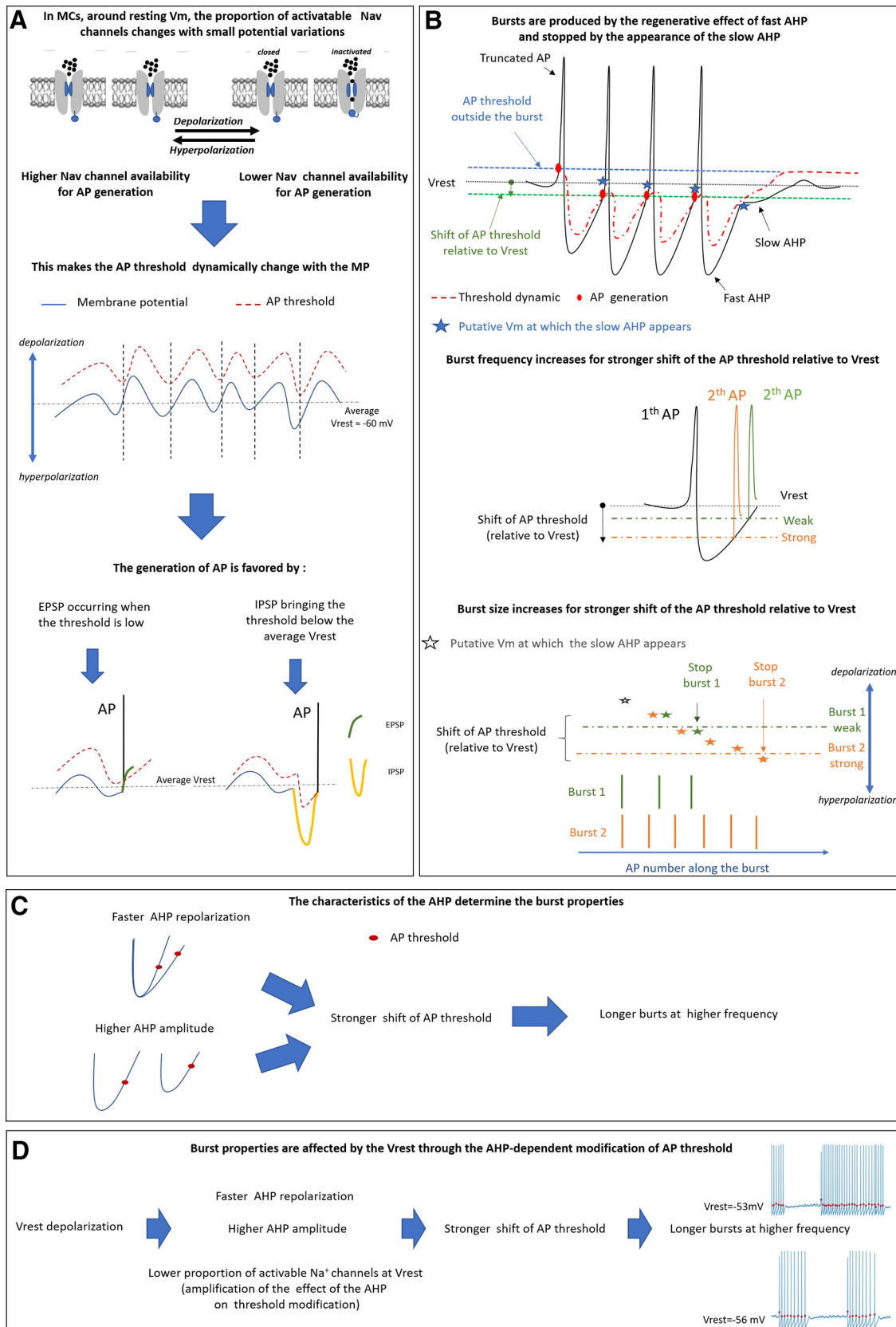


**Figure 10.** Model of the intrinsic mechanisms accounting for MC firing. **A**, Transitions of  $Na_v$  channel between deinactivated and inactivated make the AP threshold dependent on  $V_m$  fluctuations. Because of the delayed deinactivation/inactivation kinetics, the threshold fluctuation (red dashed line) is slightly shifted compared with  $V_m$  fluctuations (blue line). The generation of the AP is

*continued*

favored by excitatory inputs occurring just after the negative phase of  $V_m$  fluctuations or when the repolarization phase of inhibitory inputs is rapid enough to overcome the shifted threshold before the latter goes back to the pre-AP values. **B**, The fast AHP brings the AP threshold below the  $V_{rest}$ , and its repolarization rate is rapid enough to overcome the modified threshold, acting in this way as a regenerative mechanism that sustains the burst. The slow components of the AHP develop gradually along the successive APs. When the  $V_m$  at which the slow component should appear is above the shift of AP threshold, the manifestation of the slow component is bypassed by the AP generation. Indeed, the slow AHP can manifest itself only at a  $V_m$  value more negative than the AP threshold shift. When this happens, the  $V_m$  repolarization during the slow component is not fast enough to overcome the AP threshold, which then returns to the preburst value, and the burst stops. For a stronger shift, the AP threshold is reached earlier, during the repolarization phase of the fast AHP, and the intraburst frequency is higher. For a stronger shift of AP threshold, a higher number of APs is necessary so that the slow AHP could manifest itself and, thus, the burst duration increases. **C**, The threshold shift is larger when the fast AHP is larger and faster. In such conditions, the bursts are longer and have higher intraburst frequency. **D**, The AP threshold shift is larger when the  $V_{rest}$  of the MC is more depolarized, because of modifications of AHP properties and partial inactivation of  $Na_v$  channels. As a consequence,  $V_m$  depolarization makes bursts longer and with higher intraburst frequency.

the  $V_{rest}$ . The larger the modifications of the AP threshold, the larger the bursts (in terms of the number of APs) and the higher the intraburst firing frequencies (Fig. 10C). Indeed, the firing frequency increases because the AP threshold is reached faster during the AHP repolarization phase, especially when the shift of the AP threshold toward hyperpolarizing values is associated with faster AHP repolarization. In addition to burst size increases, the AHP slow component needs more APs to manifest itself at  $V_m$ , more negative than the AP threshold (Fig. 10B, middle and bottom panels). Finally, because the shift of the AP threshold during the burst is driven by the AHP, the burst properties are determined by the AHP features. In particular, the number of APs and firing frequency increase when the AHP amplitude and repolarization rate increase. The model also predicts the increases of burst length and intraburst frequency that we observed on membrane depolarization (Fig. 10D). In this condition, the AHP amplitude increases, possibly because of an increase of  $K^+$  driving force, and the AHP repolarization becomes faster, by an as yet unknown mechanism. Moreover, on membrane depolarization, the number of inactivated  $Na_v$  channels is augmented. As a consequence, the recovery from inactivation of  $Na_v$  channels produced by the AHP entails a larger shift of AP threshold relative to  $V_{rest}$ . In fact, our neuron computational model showed that a decrease of the number of  $Na_v$  channels available entails an increase of the hyperpolarization-induced shift in AP threshold (Fig. 5C,D, Extended Data Fig. 7-1G,H).

Altogether, the heterogeneity of the firing properties observed among the different MCs would therefore be mainly because of differences in the shapes of their AHP components, as well as the recent history of  $V_m$  values.

However, our model does not predict the minority of intraburst APs for which the threshold was clearly above the  $V_{rest}$  (Fig. 6A, right). A mechanism that could account for these events is the rebound depolarization that was frequently observed at the end of the AHP. Obviously, when it could be detected, the rebound depolarization did not overcome the AP threshold, but a great variability in the rebound amplitudes was observed, supporting the above hypothesis. The post-AHP rebound depolarization is possibly because of the activation of persistent  $Na^+$  current (Balu and Strowbridge, 2007).

Not only depicting our own results, our model fits with others reported in the literature. As an example, the tufted cells of the olfactory bulb, which present an AHP with larger amplitude and faster repolarization rate than MCs, show a more sustained bursting activity; namely, longer and higher-frequency bursts (Burton and Urban, 2014). Similar covariation between AHP and burst properties have been also reported in MCs during postnatal development (Yu et al., 2015). Our model predicts that these covariations are the consequence of AHP-dependent modifications of the AP threshold shifts. In agreement with our hypothesis of the involvement of  $I_A$  current in burst termination, the application of 4AP has been reported to transform MC bursting activity into continuous firing activity (Balu et al., 2004). MCs present a dendritic recurrent synaptic transmission that is characterized by a glutamatergic autoexcitation (Aroniadou-Anderjaska et al., 1999; Friedman and Strowbridge, 2000; Salin et al., 2001) and a feedback inhibition that follows the activation of granular cells (Isaacson and Strowbridge, 1998; Schoppa et al., 1998). It has been shown that the main effect of recurrent synaptic transmission is to shape the AHP of MCs (Duménieu et al., 2015). In particular, the recurrent inhibition increases the amplitude of the AHP without affecting the medium or the late AHP, while the recurrent excitation reduces both the amplitude and the medium component of the AHP (Duménieu et al., 2015; Fig. 5D). Based on the present results, we can therefore propose that recurrent synaptic inhibition would favor long bursts at higher firing frequency; by contrast, the functional role of recurrent excitation is less predictable. Indeed, while the reduction of the AHP amplitude would favor short bursts at low frequency, we do not know whether, and to what extent, the reduction of the medium component would affect the velocity of the repolarization phase of the AHP; further analysis on this aspect is needed to elucidate the role of recurrent excitation on MC firing properties.

The interpretation of some of our experimental results requires further discussion: in particular, the contribution of  $I_A$  in the AHP course (Fig. 9) and the role of the recovery of the sodium channel in the modification of AP threshold (Fig. 5). As evidenced from Figure 9, an increase in AHP amplitude was observed when the number of evoked consecutive APs increased. This appeared as mainly based on the increase of the 4AP-dependent AHP component. Noteworthy was that during spontaneous bursts

we did not observe any increase of AHP amplitude (Extended Data Fig. 8-1A). One possible explanation is that  $I_A$  currents develop earlier when the APs are evoked by experimental depolarizing steps, with the latter having a long duration (3 ms), relative to the AP half-width (~0.7 ms). Moreover, the depolarizing step could mask the actual starting point of the AHP, giving the impression that the  $I_A$  component was already present at the beginning of the AHP. It is therefore plausible that during spontaneous firing activity  $I_A$  appears early enough to affect the medium/slow AHP, and therefore slows down the AHP repolarization during the burst, but too late to affect the amplitude of the AHP. The hypothesis of the involvement of the recovery from inactivation of  $Na_v$  in threshold modifications implies an increase of the effect of hyperpolarization when the global availability of  $Na_v$  channels is reduced (Fig. 5B,C). This was confirmed by the application of TTX at 20 nM but not when TTX was used at 10 nM. However, TTX 10 nM application is enough to reduce the  $Na_v$  channels availability as the AP threshold was shifted positively in this condition (Extended Data Fig. 5-1). The absence of the effect with TTX at 10 nM is probably not a consequence of sampling variability (i.e., a false-negative result) since Bayesian analysis supports an actual absence of the effect ( $BF_{10}$  less than one-third; Keyzers et al., 2020). Moreover, when selecting only neurons for which both 10 and 20 nM TTX were applied, the 20 nM concentration reliably increased the effect of the  $V_m$  hyperpolarization on AP threshold while the 10 nM did not (data not shown). A plausible interpretation of these results is that the recovery from inactivation—produced by membrane hyperpolarization—may involve only those of the different subtypes of  $Na_v$  channels having a low sensitivity to TTX, thus not yet blocked at 10 nM. Further investigations are needed to confirm such a hypothesis, for example, by using selective antagonists of the different  $Na_v$  subtypes.

Last, our extensive analysis of the mechanisms that govern the discharge properties of MCs leads to the question of the functional significance and impact of these properties. The heterogeneity of the firing properties reported here confirmed previous reports of MC recordings *in vivo* and *in vitro* (Rinberg et al., 2006; Padmanabhan and Urban, 2010; Kollo et al., 2014; Leng et al., 2014). It has been proposed that such a diversity reduces the correlation of firing between different MCs to a correlated input, in this way increasing the information content of MC population activity (Padmanabhan and Urban, 2010). Moreover, computational simulations suggest that MC firing heterogeneity allows a more efficient and robust coding of stimulus information (Tripathy et al., 2013) and increases the synchronicity of MC firing when the correlation between the inputs is low, by possibly promoting encoding of odor combinations acting on different types of sensory receptors (Zhou et al., 2013). Our results show that the diversity among the population of MCs is largely determined by the heterogeneity of the AHP characteristics, which play a pivotal role in determining the properties of MC firing activity. However, the AHP characteristics can be directly altered by the membrane potential (present work), neuromodulation (Wu et al., 2002; Brosh et al., 2006), postnatal development (Duménieu et al.,

2015; Yu et al., 2015), learning (Duménieu et al., 2015; Reuveni and Barkai, 2018), and recurrent synaptic transmission (Duménieu et al., 2015). Therefore, thanks to highly scalable characteristics, the AHP appears to be a key target for the modulation of olfactory bulb processing according to many parameters such as physiological state (e.g., reproduction period and food need), memory, and experience.

## References

- Adelman JP, Maylie J, Sah P (2012) Small-conductance  $Ca^{2+}$ -activated  $K^+$  channels: form and function. *Annu Rev Physiol* 74:245–269.
- Amendola J, Woodhouse A, Martin-Eauclaire M-F, Goillard J-M (2012)  $Ca^{2+}$ /cAMP-sensitive covariation of  $I_A$  and  $I_H$  voltage dependences tunes rebound firing in dopaminergic neurons. *J Neurosci* 32:2166–2181.
- Andrade R, Foehring RC, Tzingounis AV (2012) The calcium-activated slow AHP: cutting through the Gordian knot. *Front Cell Neurosci* 6:47.
- Aroniadou-Anderjaska V, Ennis M, Shipley MT (1999) Dendrodendritic recurrent excitation in mitral cells of the rat olfactory bulb. *J Neurophysiol* 82:489–494.
- Azouz R, Gray CM (2003) Adaptive coincidence detection and dynamic gain control in visual cortical neurons *in vivo*. *Neuron* 37:513–523.
- Balu R, Strowbridge BW (2007) Opposing inward and outward conductances regulate rebound discharges in olfactory mitral cells. *J Neurophysiol* 97:1959–1968.
- Balu R, Larimer P, Strowbridge BW (2004) Phasic stimuli evoke precisely timed spikes in intermittently discharging mitral cells. *J Neurophysiol* 92:743–753.
- Brosh I, Rosenblum K, Barkai E (2006) Learning-induced reversal of the effect of noradrenalin on the postburst AHP. *J Neurophysiol* 96:1728–1733.
- Burton SD, Urban NN (2014) Greater excitability and firing irregularity of tufted cells underlies distinct afferent-evoked activity of olfactory bulb mitral and tufted cells. *J Physiol* 592:2097–2118.
- Cain SM, Snutch TP (2010) Contributions of T-type calcium channel isoforms to neuronal firing. *Channels (Austin)* 4:475–482.
- Chen WR, Shepherd GM (1997) Membrane and synaptic properties of mitral cells in slices of rat olfactory bulb. *Brain Res* 745:189–196.
- Deister CA, Chan CS, Surmeier DJ, Wilson CJ (2009) Calcium-activated SK channels influence voltage-gated ion channels to determine the precision of firing in globus pallidus neurons. *J Neurosci* 29:8452–8461.
- Desmairons D, Vincent JD, Lledo PM (1999) Control of action potential timing by intrinsic subthreshold oscillations in olfactory bulb output neurons. *J Neurosci* 19:10727–10737.
- Duménieu M, Fourcaud-Trocmé N, Garcia S, Kuczewski N (2015) Afterhyperpolarization (AHP) regulates the frequency and timing of action potentials in the mitral cells of the olfactory bulb: role of olfactory experience. *Physiol Rep* 3:e12344.
- Faber ESL, Sah P (2007) Functions of SK channels in central neurons. *Clin Exp Pharmacol Physiol* 34:1077–1083.
- Friedman D, Strowbridge BW (2000) Functional role of NMDA autoreceptors in olfactory mitral cells. *J Neurophysiol* 84:39–50.
- Henze DA, Buzsáki G (2001) Action potential threshold of hippocampal pyramidal cells *in vivo* is increased by recent spiking activity. *Neuroscience* 105:121–130.
- Hu W, Tian C, Li T, Yang M, Hou H, Shu Y (2009) Distinct contributions of  $Na_v1.6$  and  $Na_v1.2$  in action potential initiation and back-propagation. *Nat Neurosci* 12:996–1002.
- Isaacson JS, Strowbridge BW (1998) Olfactory reciprocal synapses: dendritic signaling in the CNS. *Neuron* 20:749–761.



- Iyer R, Ungless MA, Faisal AA (2017) Calcium-activated SK channels control firing regularity by modulating sodium channel availability in midbrain dopamine neurons. *Sci Rep* 7:5248.
- JASP Team (2020) JASP (Version 0.14.1) [Computer software].
- Keyzers C, Gazzola V, Wagenmakers EJ (2020) Using Bayes factor hypothesis testing in neuroscience to establish evidence of absence. *Nat Neurosci* 23:788–799.
- Kollo M, Schmaltz A, Abdelhamid M, Fukunaga I, Schaefer AT (2014) “Silent” mitral cells dominate odor responses in the olfactory bulb of awake mice. *Nat Neurosci* 17:1313–1315.
- Leng G, Hashimoto H, Tsuji C, Sabatier N, Ludwig M (2014) Discharge patterning in rat olfactory bulb mitral cells in vivo. *Physiol Rep* 2:e12021.
- Li T, Tian C, Scalmani P, Frassoni C, Mantegazza M, Wang Y, Yang M, Wu S, Shu Y (2014) Action potential initiation in neocortical inhibitory interneurons. *PLoS Biol* 12:e1001944.
- Padmanabhan K, Urban NN (2010) Intrinsic biophysical diversity decorrelates neuronal firing while increasing information content. *Nat Neurosci* 13:1276–1282.
- Platkiewicz J, Brette R (2011) Impact of fast sodium channel inactivation on spike threshold dynamics and synaptic integration. *PLoS Comput Biol* 7:e1001129.
- Reuveni I, Barkai E (2018) Tune it in: mechanisms and computational significance of neuron-autonomous plasticity. *J Neurophysiol* 120:1781–1795.
- Rinberg D, Koulakov A, Gelperin A (2006) Sparse odor coding in awake behaving mice. *J Neurosci* 26:8857–8865.
- Rubin DB, Cleland TA (2006) Dynamical mechanisms of odor processing in olfactory bulb mitral cells. *J Neurophysiol* 96:555–568.
- Sah P, Faber ESL (2002) Channels underlying neuronal calcium-activated potassium currents. *Prog Neurobiol* 66:345–353.
- Salin PA, Lledo PM, Vincent JD, Charpak S (2001) Dendritic glutamate autoreceptors modulate signal processing in rat mitral cells. *J Neurophysiol* 85:1275–1282.
- Schoppa NE, Kinzie JM, Sahara Y, Segerson TP, Westbrook GL (1998) Dendrodendritic inhibition in the olfactory bulb is driven by NMDA receptors. *J Neurosci* 18:6790–6802.
- Schwindt PC, Spain WJ, Foehring RC, Stafstrom CE, Chubb MC, Crill WE (1988) Multiple potassium conductances and their functions in neurons from cat sensorimotor cortex in vitro. *J Neurophysiol* 59:424–449.
- Tripathy SJ, Padmanabhan K, Gerkin RC, Urban NN (2013) Intermediate intrinsic diversity enhances neural population coding. *Proc Natl Acad Sci U S A* 110:8248–8253.
- Wu WW, Oh MM, Disterhoft JF (2002) Age-related biophysical alterations of hippocampal pyramidal neurons: implications for learning and memory. *Ageing Res Rev* 1:181–207.
- Yu Y, Burton SD, Tripathy SJ, Urban NN (2015) Postnatal development attunes olfactory bulb mitral cells to high-frequency signaling. *J Neurophysiol* 114:2830–2842.
- Zhou P, Burton S, Urban N, Ermentrout GB (2013) Impact of neuronal heterogeneity on correlated colored noise-induced synchronization. *Front Comput Neurosci* 7:113.